Distributed and Risk-averse ADP Algorithm for Stochastic Economic Dispatch of Power System with Multiple Offshore Wind Farms

Xiangyong Feng, Shunjiang Lin, *Senior Member*, *IEEE*, *Senior Member*, *CSEE*, Yutao Liang, Guansheng Fan, and Mingbo Liu, *Member*, *IEEE*, *Senior Member*, *CSEE*

***Abstract*—With more and more offshore wind power being increasingly connected to power grids, fluctuations in offshore wind speeds result in risks of high operation costs. To mitigate this problem, a risk-averse stochastic economic dispatch (ED) model of power system with multiple offshore wind farms (OWFs) is proposed in this paper. In this model, a novel GlueVaR method is used to measure the tail risk of the probability distribution of operation cost. The weighted sum of the expected operation cost and the GlueVaR is used to reflect the risk of operation cost, which can consider different risk requirements including risk aversion and risk neutrality flexibly by adjusting parameters. Then, a risk-averse approximate dynamic programming (ADP) algorithm is designed for solving the proposed model, in which multi-period ED problem is decoupled into a series of single-period ED problems. Besides, GlueVaR is introduced into the approximate value function training process for risk aversion. Finally, a distributed and risk-averse ADP algorithm is constructed based on the alternating direction method of multipliers, which can further decouple single-period ED between transmission system and multiple OWFs for ensuring information privacy. Case studies on the modified IEEE 39-bus system with an OWF and an actual provincial power system with four OWFs demonstrate correctness and efficiency of the proposed model and algorithm.**

***Index Terms*—Approximate dynamic programming (ADP), alternating direction method of multipliers, GlueVaR, offshore wind farm, risk-averse stochastic optimization.**

NOMENCLATURE

A. Sets and Indices

t/Ω_{T}	Index/Sets of all time periods.
g/Ω_{G}	Index/Sets of fuel-fired units in power system.
m/Ω_{OWF}	Index/Sets of OWFs.
w/Ω_m	Index/Sets of wind turbines in the m-th OWF.
s/N_{s}	Index/Sets of storage units.
p/N_{ps}	Index/Sets of PSH stations in power system.
$b/N_{\mathrm{bs},m}$	Index/Sets of BS stations in m-th OWF.
$r/B_p/B_b$	Index/Sets of piecewise storage quantities of PSH/BS station.
c_m/N_{con}	Index/Sets of connection buses between power system and OWFs.
i/j	Indices of buses.
ij	Index of branches.
$\delta(j)/\pi(j)$	Set of buses whose parent/child bus is bus j.

B. Parameters

$C_{\mathrm{W}m}$	Penalty cost coefficient of wind curtailment.
a_{lg}/e_{lg}	Slope/Intercept of the l_g-th segment of the piecewise linear cost function of the g-th thermal power unit.
$P_{g,\min}/P_{g,\max}$	Minimum/Maximum active output of the g-th thermal power unit.
$r_{g,\mathrm{u}}/r_{g,\mathrm{d}}$	Ramp up/down rate of the g-th thermal power unit.
ΔT	Length of a time period, i.e., 1 h in this article.
$\theta_{ij,\min}/\theta_{ij,\max}$	Minimum/Maximum value of θ_{ij}.
$P_{\mathrm{L}i,t}$	Active load power of bus i.
η_p/η_b	Roundtrip efficiency of PSH/BS station.
$P_{\mathrm{pp},\max}/P_{\mathrm{gp},\max}$	Maximum pumping/generating output of the p-th PSH station.
$P_{\mathrm{cb},\max}/P_{\mathrm{db},\max}$	Maximum charging/discharging output of the b-th BS station.
$P_{ij,\min}/P_{ij,\max}$	Minimum/Maximum active power of branch ij.
$R_{p,\min}/R_{p,\max}$	Minimum/Maximum stored energy of the upper reservoir of the p-th PSH station.
$R_{b,\min}/R_{b,\max}$	Minimum/Maximum stored energy of the b-th BS station.
b_{ij}	Susceptance of branch ij.
r_{ij}/x_{ij}	Resistance/Reactance of branch ij.
θ_s	Weight of the s-th storage unit.
$P_{wj\min}$	Minimum active power output of wind turbine w.
$P_{wj\max,t}$	Maximum available active power output of wind turbine w at time period t.

Manuscript received June 13, 2022; revised August 5, 2022; accepted August 23, 2022. Date of online publication June 27, 2023; date of current version June 5, 2024. This work was supported by the Key Research and Development Project of Guangdong Province (2021B0101230004) and the National Natural Science Foundation of China (51977080).

X. Y. Feng, S. J. Lin (corresponding author, email: linshj@scut.edu.cn), Y. T. Liang and M. B. Liu are with the School of Electric Power Engineering, South China University of Technology, Guangzhou 510640, China, and the Guangdong Key Laboratory of Clean Energy Technology, South China University of Technology, Guangzhou 511458, China.

G. S. Fan is with the Guangzhou Power Supply Bureau, Guangdong Power Grid Co., Ltd., Guangzhou 510000, China.

DOI: 10.17775/CSEEJPES.2022.03890

$\tilde{I}_{ij,\max}$	Maximum square of current of branch ij.
$\tilde{U}_{j,\min}/\tilde{U}_{j,\max}$	Minimum/Maximum square of voltage of bus j.
$\varphi_{\min}/\varphi_{\max}$	Minimum/Maximum power factor angle of wind turbine w.
$C_{\mathrm{p}w}/C_{\mathrm{T}w}$	Power coefficient/Thrust coefficient of wind turbine w.
P_{rated}	Rated active power of wind turbine g.
ρ_{a}	Air density.
$v_{\mathrm{ci}}/v_{\mathrm{rated}}/v_{\mathrm{co}}$	Cut-in/Rated/Cut-out wind speed of wind turbine g.
$R_{w'w}$	Wake radius generated by the wind turbine w' at wind turbine w along the wind direction.
v_m	Natural wind speed of the OWF m.
R	Rotor radius of all wind turbines.
α	Wake decay constant, the recommended value of which is 0.04 for the offshore environment.
d	Distance between the wake area center and WT rotation area.
$X_{w'w}$	Distance between wind turbines w' and w along wind direction.
$\varepsilon_1/\varepsilon_2$	Threshold of the stop criterion of ADMM algorithm.
λ_1/λ_2	Augmented Lagrange multiplier.
ρ	Penalty coefficient.
M	Total number of OWFs.

C. Variables

$F_{g,t}$	Operation cost of thermal power unit g.
$P_{g,t}$	Active power output of thermal power unit g.
$P_{i,t}$	Injected active power of bus i at period t.
$P_{j,t}$	Injected active power of bus j at period t in the OWF.
$R_{p,t}/R_{b,t}$	Stored energy of PSH/BS station at period t.
$P_{\mathrm{pp},t}/P_{\mathrm{gp},t}$	Pumping/Generating power of PSH station at period t.
$y_{\mathrm{pp},t}/y_{\mathrm{gp},t}$	Binary variable indexing the pumping/generating state of PSH station at period t.
$P_{\mathrm{cb},t}/P_{\mathrm{db},t}$	Charging/Discharging power of BS station at period t.
$y_{\mathrm{cb},t}/y_{\mathrm{db},t}$	Binary variable indexing the charging/discharging state of BS station at period t.
$P_{ij,t}/Q_{ij,t}$	Active/Reactive power in the head end of branch ij at period t.
$\tilde{U}_{j,t}$	Square of the voltage of bus j at period t.
$\tilde{I}_{ij,t}$	Square of the current of branch ij at period t.
$P_{wj,t}/Q_{wj,t}$	Active/Reactive power outputs of wind turbine w in bus j at period t.
$P_{\mathrm{Wc},m}/P_{\Sigma\mathrm{c},m}$	Active power across the connection bus cm between transmission system and m-th OWF.
$\boldsymbol{v}_t$	Vector of stochastic variables at period t.
$\boldsymbol{R}_t$	Vector of storage quantities at period t.
$\boldsymbol{S}_t/\boldsymbol{x}_t$	Vector of state/decision variables at period t.
$\boldsymbol{x}_1/\boldsymbol{x}_2$	Variables of region 1/2.
$x_{1\mathrm{bc}}/x_{2\mathrm{bc}}$	Boundary coupling variables of region 1/2.
$\boldsymbol{z}$	Intermediate variables in the ADMM.
c_1/c_2	Cost function of region 1/2.

I. INTRODUCTION

WITH power generated from offshore wind farms (OWFs) increasingly being integrated into power grids, wind speed uncertainties considerably affect active power outputs of OWFs and render the secure and economic operation of the power system with multiple OWFs challenging [1], [2]. To address power uncertainties, storage systems such as pumped-storage hydro (PSH) stations and battery storage (BS) stations are widely used in transmission systems and OWFs, respectively, which play a crucial role in the economic dispatch (ED) of power systems [3]. Furthermore, the performance of the transmission system and multiple OWFs are attributed to various stakeholders, including the power network company and OWF investment companies. Therefore, ensuring information privacy between the transmission system and multiple OWFs is crucial. Thus, the ED problem of power systems with multiple OWFs considering wind speed uncertainties has attracted considerable research attention.

Robust optimization (RO) and stochastic optimization (SO) are typically used to mitigate the effects of uncertainty on the ED problem. In RO [4], [5], decisions are made under the worst case of given uncertainty sets of uncertain variables. However, these decision results are too conservative because the worst-case scenario does not always occur [6]. In SO [7]–[9], uncertainty in optimization problems is addressed by describing uncertain variables with a series of sampling scenarios [10]. However, SO decision results could be over-optimistic and risk-neutral because low-probability, high-impact uncertainty scenarios are usually excluded via the scenario reduction methods for alleviating computational burden [11].

To avoid potential risks of decision results due to uncertain variables, numerous studies have focused on integrating appropriate risk measures into the SO method to avoid over-optimistic decisions [12]–[17]. In [12] and [13], an adaptive risk-averse SO approach for multi-energy microgrids and risk-based scheduling and control of microgrids under uncertainty were presented, respectively, by scenario-based method, in which conditional value-at-risk (CVaR)-based risk-measurement method was used to avoid over-optimistic solutions. In [14], the robustness function of the information gap decision method was used for developing the risk-averse strategy to appropriately manage fluctuations of uncertain parameters of microgrids. In [15] and [16], the risk-averse stochastic programming model for the hybrid wind-thermal power system and voltage control of AC/DC power systems was proposed, respectively. The risk-aversion procedure was formulated using CVaR. In [17], uncertainties were modeled using a scenario-based stochastic approach, whereas risk-related uncertainties were modeled by using downside risk constraints to capture risk-averse operations. Among these publications, CVaR is the most popular risk-measurement method used in the risk-averse framework. In fact, decision-makers always consider two conflicting demands and try to make a balance between them. On one hand, aversion to high economic risks of some extreme scenarios is critical. On the other hand, they also wish to reduce the operation cost of the forecast scenario. However, the conservatism of CVaR risk measurement can only be adjusted by changing the given confidence level, which makes it difficult to find a satisfactory degree of risk aversion. Recently, a novel flexible risk-measurement method based on distortion function called GlueVaR was proposed in the financial field to utilize more than one parameter to capture various risk demands [18]. Conservatism of GlueVaR can be adjusted not only by changing confidence level but also by changing other parameters. By selecting appropriate parameters, GlueVaR can be a combination of value-at-risk (VaR) and CVaR, which makes GlueVaR more flexible in reflecting risk aversion degree than CVaR. Thus, GlueVaR will be further studied and applied in the ED problem of a power system with multiple OWFs for risk aversion decisions in this paper.

Besides, the aforementioned studies [12]–[17] have mostly utilized scenario-based methods to establish SO model, which is only suitable for microgrids and small-scale power systems. However, the computational burden increases rapidly when the system is large or numerous scenarios are taken into account [19]. The approximate dynamic programming (ADP) algorithm exhibits excellent computational performance for the stochastic ED (SED) problem with storage systems. The multi-period SED problem is transformed into a series of single-period ED problems by approximate value functions (AVFs), which can effectively reduce model scale [20]. In [21] and [22], the ADP algorithm was applied to solve the SED problem of microgrids and residential distributed energy systems. However, the aforementioned ADP formulation for the SED problem is risk neutral, and decisions may have the risk of high operation cost due to fluctuations in uncertain variables, which makes it critical to introduce a proper risk-measurement method into the ADP formulation for avoiding this risk. Therefore, a risk-averse ADP algorithm with GlueVaR is proposed in this paper. In addition, the conventional ADP algorithm requires a relatively long time to train AVFs, which should be improved in the proposed risk-averse ADP algorithm.

For a power system with multiple OWFs, the transmission systems and each OWF are connected by the same connection bus. Information privacy is a critical requirement between the transmission systems and multiple OWFs, which renders the realization of the centralized optimization method difficult [23]. Furthermore, the centralized optimization method requires data from the power system and increases the computational burden on the central control center when considerable data form multiple OWFs exist [24]. Therefore, the distributed optimization method is suitable for the SED of a power system with multiple OWFs. The alternating direction method of multipliers (ADMM) is a widely used distributed optimization method in which the decomposability of the dual ascending algorithm and the convergence of multiplier method are combined [25]. This method has been extensively applied in ED [26], voltage control [23], and optimal power flow [27]. However, further research is required in combining the ADMM and risk-averse ADP algorithm and designing the distributed risk-aversion optimization algorithm for solving the SED of a power system with multiple OWFs.

The major contributions of the present study are as follows:

1) Considering uncertainties of offshore wind speeds and introducing a novel risk-measurement method, GlueVaR, a risk-averse SED model of power system with multiple OWFs, PSH stations, and BS stations, is established. The relationship between wind speeds and maximum available active outputs of wind turbines is calculated by using the wake model.

2) A risk-averse ADP algorithm is proposed to solve the risk-averse SED model by introducing the GlueVaR-based risk-averse method in the training process of AVFs. It can solve multiple scenarios of the same group by parallel computing in AVF training, which improves computational efficiency compared with conventional ADP algorithm. It can also avert the potential risk of high operation costs in some extreme scenarios and narrow the range of operation costs under wind speed uncertainties.

3) A distributed and risk-averse ADP algorithm combining risk-averse ADP and ADMM algorithm is proposed to solve the proposed SED model by distributed optimization calculation between the transmission system and multiple OWFs. This technique can maintain information privacy between transmission system and multiple OWFs.

The rest of this paper is organized as follows: Section II introduces the risk-measurement method based on GlueVaR. Section III proposes a risk-averse SED model for a power system with multiple OWFs. Section IV introduces the distributed and risk-averse ADP algorithm for solving the proposed model. Section V presents case studies in the modified IEEE 39-bus system and an actual provincial power system. Section VI presents the conclusion.

II. Risk-Measurement Method Based on GlueVaR

To calculate risk-measurement cost, selecting an appropriate risk-measurement method is crucial. VaR and CVaR are the most widely used risk measures. VaR does not consider the tail risk cost of the probability density function (PDF) of the random variable. CVaR can consider tail risk cost of the PDF and quantify risk potential beyond VaR, which has been widely used in many fields [12]. Calculations of VaR and CVaR are as follows:

$$\mathrm{VaR}_\alpha(X) = \inf_u \{P(X \le u) \ge \alpha\} \tag{1}$$

$$\mathrm{CVaR}_\alpha(X) = \inf_u \{u + 1/(1-\alpha)E[(X-u)^+]\} \tag{2}$$

where $\alpha \in [0, 1]$ is confidence level; $P(X \le u) \ge \alpha$ indicates the probability of random variable X is lower than u is greater than α; $(X-u)^+$ denotes the value is $X-u$ when $X \ge u$, and value is 0 when $X \le u$.

GlueVaR is a risk-measurement method with multiple parameters, which is flexible and convenient for finding the appropriate combination of parameters to reflect multiple risk demands. Selecting appropriate parameters can cover various risk-measurement methods including VaR and CVaR. Some basic definitions related to GlueVaR are as follows:

Definition 1. Let g: $[0,1] \to [0,1]$ be a function such that $g(0)=0$, $g(1)=1$, and g is non-decreasing. Then g is called a distortion function.

Definition 2. Let g be a distortion function. Consider a random variable X and its survival function $S_X(x)=P(X>x)$. Function $\rho_g(X)=\int_{-\infty}^{0}[g(S_X(x))-1]\mathrm{d}x+\int_{0}^{+\infty}g(S_X(x))\mathrm{d}x$ is called a distortion risk measure.

Given two confidence levels α and β, the distortion function of GlueVaR is expressed as (3) VaR_α and CVaR_α can be described by their distortion functions. Further details can be found in [18].

$$g_{\beta,\alpha}^{h_1,h_2}(u)=\begin{cases} h_1/(1-\beta)\times u, & 0\le u<1-\beta \\ h_1+\dfrac{h_2-h_1}{\beta-\alpha}\times[u-(1-\beta)], & 1-\beta\le u<1-\alpha \\ 1, & 1-\alpha\le u<1 \end{cases} \tag{3}$$

where α, $\beta\in[0,1]$, $\alpha<\beta$; $h_1\in[0,1]$, and $h_2\in[h_1,1]$.

If the following notation is used,

$$\begin{cases} k_1=h_1-(h_2-h_1)\times(1-\beta)/(\beta-\alpha) \\ k_2=(h_2-h_1)/(\beta-\alpha)\times(1-\alpha) \\ k_3=1-k_1-k_2 \end{cases} \tag{4}$$

then, according to [18], distortion function $g_{\beta,\alpha}^{h_1,h_2}(u)$ can be rewritten as follows:

$$g_{\beta,\alpha}^{h_1,h_2}(u)=k_1\gamma_\beta(u)+k_2\gamma_\alpha(u)+k_3\psi_\alpha(u) \tag{5}$$

where γ_β, γ_α, and ψ_α are distortion functions of CVaR at confidence levels β and α, and of VaR at confidence level α, respectively. Therefore, GlueVaR risk measure $\kappa_{\beta,\alpha}^{k_1,k_2}(X)$ can be expressed as a linear combination of three risk measures: CVaR at confidence levels α and β, and VaR at confidence level α, as follows:

$$\kappa_{\beta,\alpha}^{k_1,k_2}(X)=k_1\mathrm{CVaR}_\beta(X)+k_2\mathrm{CVaR}_\alpha(X)+k_3\mathrm{VaR}_\alpha(X) \tag{6}$$

The main differences between VaR, CVaR, and GlueVaR are shown in Fig. 1. Unlike VaR and CVaR, which can only make decisions under a single parameter, GlueVaR includes the following three conditions when confidence levels α and β are given: a) The most conservative situation at CVaR_β; b) The general conservative situation at CVaR_α; and c) The general situation at VaR_α. Thus, in GlueVaR, the risk cost of extreme scenarios in the tail of the PDF of a random variable is considered.

Given confidence levels α and β, risk measure GlueVaR satisfies subadditivity in the tail and becomes a coherent measure within a specific range [18], from which convexity of GlueVaR can be deduced [28]. The range of (k_1, k_2) value which makes $\kappa_{\beta,\alpha}^{k_1,k_2}(X)$ satisfy subadditivity in the tail is the shaded in Fig. 2. From(4) when k_1 and k_2 are given, k_3 can be calculated. The closer the weight (k_1, k_2) is to the point $(\frac{1-\beta}{1-\alpha},0)$, the greater the weight of $\mathrm{VaR}_\alpha k_3$ is, and the decision is inclined to a lower risk-averse level. When weight (k_1, k_2) falls on the red line in Fig. 2, the weight of $\mathrm{VaR}_\alpha k_3$ is zero,

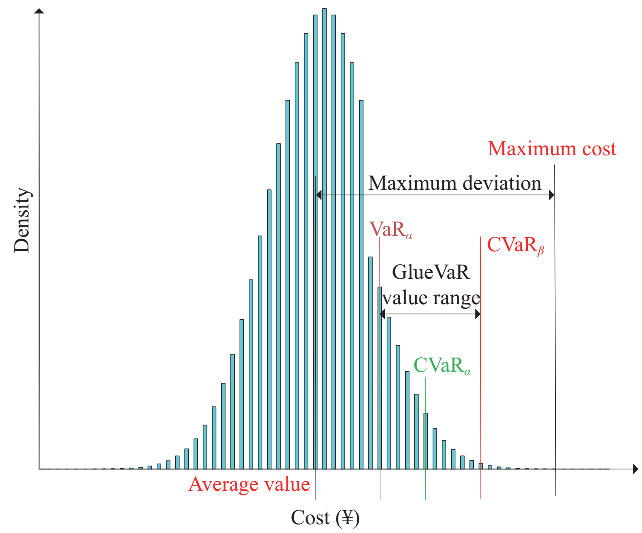

Fig. 1. Schematic of the differences between VaR, CVaR, and GlueVaR.

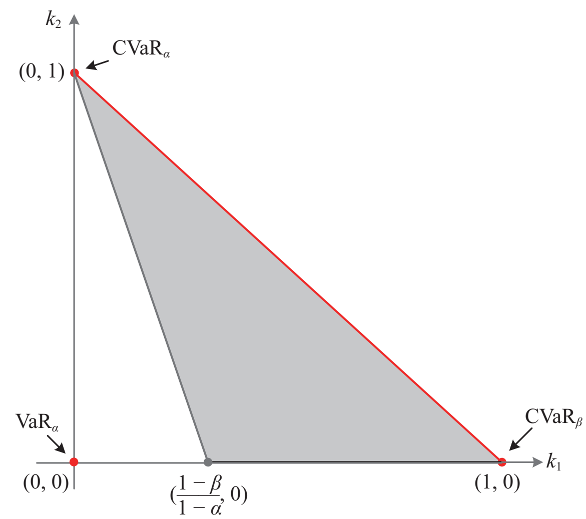

Fig. 2. Value range of (k_1, k_2) after giving α and β.

which indicates the decision is at a higher risk-averse level and more conservative. On this red line, risk-averse level of the decision is higher when weight (k_1, k_2) is closer to (1, 0), whereas risk-averse level of the decision is lower when weight (k_1, k_2) is closer to (0, 1). Therefore, by adjusting the two parameters k_1 and k_2 after giving confidence levels α and β, weights of different risk measures in the GlueVaR can be adjusted according to various risk-aversion requirements.

III. Risk-Averse SED Model of Power System with Multiple OWFs

For a power system with multiple OWFs, the transmission system includes thermal power units and PSH stations, and OWFs include wind turbines (WTs) and BS stations. The risk-averse SED model of such a system is described as follows.

A. Objective Function

The objective function of the risk-averse SED model includes the operation cost of thermal power units and wind curtailment cost in OWFs. Considering uncertainties of wind speeds in OWFs and risks of high operation cost, the objective function should be expressed as minimizing the weighted sum of the expected value of operation costs corresponding to various possible scenarios of wind speeds and risk measure cost as follows:

$$\min \sum_{t\in\Omega_{\mathrm{T}}} \rho_t^{\mathrm{risk}}(C_t) \tag{7}$$

$$\rho_t^{\mathrm{risk}}(C_t) = (1-\lambda)E(C_t) + \lambda\kappa(C_t) \tag{8}$$

$$C_t = \sum_{g\in\Omega_{\mathrm{G}}} F_{g,t} + \sum_{m\in\Omega_{\mathrm{OWF}}} \sum_{w\in\Omega_m} C_{\mathrm{W}m}(P_{wj\max,t} - P_{wj,t}) \tag{9}$$

where ρ_t^{risk} is weighted risk measure cost; λ is weight coefficient, and model becomes a risk-neutral model when $\lambda = 0$; E is mathematical expectation operator, and κ is risk measure cost. Equation (8) considers risk cost of extreme scenarios, and decision results can avert potential risk of high operation cost of some extreme scenarios.

Operation cost of thermal power units $F_{g,t}$ is a quadratic function as (10) and it can be approximated by piecewise linear inequality for higher solution efficiency [29], as shown in (11).

$$F_{g,t} = A_{g2} \times P_{g,t}^2 + A_{g2} \times P_{g,t} + A_{g0} \tag{10}$$

$$F_{g,t} \geq a_{l_g} P_{g,t} + e_{l_g},\ l_g = 1, 2, \cdots, L \tag{11}$$

B. Operation Constraints of Thermal Power Units

Thermal power units need to operate under constraints (12) as follows.

$$P_{g,\min} \leq P_{g,t} \leq P_{g,\max},\ \forall g \in \Omega_{\mathrm{G}} \tag{12}$$

$$\begin{cases} P_{g,t} - P_{g,t-1} \leq r_{g,\mathrm{u}}\Delta T \\ P_{g,t-1} - P_{g,t} \leq r_{g,\mathrm{d}}\Delta T \end{cases} \quad (t > 1) \tag{13}$$

C. Operation Constraints of PSH Stations

$$R_{p,t} = R_{p,t-1} + P_{\mathrm{pp},t}\eta_p\Delta T - P_{\mathrm{gp},t}\Delta T \tag{14}$$

$$\begin{cases} R_{p,\min} \leq R_{p,t} \leq R_{p,\max} \\ R_{p,T} = R_{p,0} \end{cases} \tag{15}$$

$$\begin{cases} y_{\mathrm{pp},t} + y_{\mathrm{gp},t} \leq 1,\ y_{\mathrm{pp},t},\ y_{\mathrm{gp},t} \in \{0,1\} \\ 0 \leq P_{\mathrm{pp},t} \leq y_{\mathrm{pp},t} P_{\mathrm{pp,max}} \\ 0 \leq P_{\mathrm{gp},t} \leq y_{\mathrm{gp},t} P_{\mathrm{gp,max}} \end{cases} \tag{16}$$

D. Security Limit of Active Power Flow of Branches

DC power flow model is used to describe transmission branches on the grid side as follows:

$$P_{ij,t} = -b_{ij}\theta_{ij,t} \tag{17}$$

$$P_{i,t} = \sum_{i\to j} P_{ij,t} \tag{18}$$

$$\begin{cases} P_{ij,\min} \leq P_{ij,t} \leq P_{ij,\max} \\ \theta_{ij,\min} \leq \theta_{ij,t} \leq \theta_{ij,\max} \end{cases} \tag{19}$$

where $\theta_{ij} = \theta_i - \theta_j$ is difference angle between bus i and j. In (18), if bus i is connected to fuel-fired units, $P_{i,t} = P_{g,t} - P_{\mathrm{L}i,t}$; if bus i is connected to OWF m, $P_{i,t} = P_{\Sigma mi,t} - P_{\mathrm{L}i,t}$; and if bus i is connected to PSH stations, $P_{i,t} = P_{\mathrm{gp},t} - P_{\mathrm{pp},t} - P_{\mathrm{L}i,t}$.

E. Operation Constraints of BS Stations

$$R_{b,t} = R_{b,t-1} + P_{\mathrm{cb},t}\eta_b\Delta T - P_{\mathrm{db},t}\Delta T \tag{20}$$

$$\begin{cases} R_{b,\min} \leq R_{b,t} \leq R_{b,\max} \\ R_{b,T} = R_{b,0} \end{cases} \tag{21}$$

$$\begin{cases} y_{\mathrm{cb},t} + y_{\mathrm{db},t} \leq 1, y_{\mathrm{cb},t}, y_{\mathrm{db},t} \in \{0,1\} \\ 0 \leq P_{\mathrm{cb},t} \leq y_{\mathrm{cb},t} P_{\mathrm{cb,max}} \\ 0 \leq P_{\mathrm{db},t} \leq y_{\mathrm{db},t} P_{\mathrm{db,max}} \end{cases} \tag{22}$$

F. Power Output Constraints of WTs

Power output constraints of WTs are as follows:

$$P_{wj\min} \leq P_{wj,t} \leq P_{wj\max,t} \tag{23}$$

$$P_{wj,t} \cdot \tan\varphi_{\min} \leq Q_{wj,t} \leq P_{wj,t} \cdot \tan\varphi_{\max} \tag{24}$$

G. Power Flow Equations of the OWF Collector Network

AC collector network in a OWF is typically a radial network. Considering ground susceptance of marine cable lines, AC collector network can be described by the branch power flow model as follows [1]:

$$\sum_{k\in\delta(j)} P_{jk,t} = \sum_{i\in\pi(j)} (P_{ij,t} - r_{ij}\tilde{I}_{ij,t}) + P_{j,t} \tag{25}$$

$$\sum_{k\in\delta(j)} Q_{jk,t} = \sum_{i\in\pi(j)} (Q_{ij,t} - x_{ij}\tilde{I}_{ij,t}) + b_j\tilde{U}_{j,t} + Q_{j,t} \tag{26}$$

$$\tilde{U}_{j,t} = \tilde{U}_{i,t} - 2(r_{ij}P_{ij,t} + x_{ij}Q_{ij,t}) + [(r_{ij})^2 + (x_{ij})^2]\tilde{I}_{ij,t} \tag{27}$$

$$\tilde{I}_{ij,t}\tilde{U}_{i,t} = (P_{ij,t})^2 + (Q_{ij,t})^2 \tag{28}$$

In (25) and (26) if bus j is connected to BS station b, then $P_{j,t} = P_{\mathrm{db},t} - P_{\mathrm{cb},t}$, $Q_{j,t} = 0$; if bus j is connected to WT w, $P_{j,t} = P_{wj,t}$, and $Q_{j,t} = Q_{wj,t}$.

Nonconvex quadratic (28) can be transformed into a convex inequality constraint using second-order cone relaxation [31] as follows:

$$\|2P_{ij,t};\quad 2Q_{ij,t};\quad \tilde{I}_{ij,t} - \tilde{U}_{i,t}\|_2 \leq \tilde{I}_{ij,t} + \tilde{U}_{i,t} \tag{29}$$

To ensure the secure operation of the OWF collector network, branch current and bus voltage should not exceed the following secure operation limit:

$$\begin{cases} 0 \leq \tilde{I}_{ij,t} \leq \tilde{I}_{ij,\max} \\ \tilde{U}_{j,\min} \leq \tilde{U}_{j,t} \leq \tilde{U}_{j,\max} \end{cases} \tag{30}$$

H. Maximum Available Active Power Output of Wind Turbine

Maximum available active power output of WT w can be expressed as follows [32]:

$$P_{wj\max} = \begin{cases} 0 & v_w < v_{\mathrm{ci}} \\ \dfrac{1}{2}\rho_{\mathrm{a}}\pi R^2 v_w^3 C_{\mathrm{pw}} & v_{\mathrm{ci}} \leq v_w < v_{\mathrm{rated}} \\ P_{\mathrm{rated}} & v_{\mathrm{rated}} \leq v_w \leq v_{\mathrm{co}} \end{cases} \tag{31}$$

where $P_{wj\max}$ can be calculated based on wind speed v_w. However, because of the wake effect, wind speeds of multiple WTs affect each other in an OWF. The Jensen model is used to describe the wake effect as follows [32]:

$$R_{w'w} = R + \alpha X_{w'w} \tag{32}$$

$$v_{w'w} = v_0\left[1-\left(1-\sqrt{1-C_{\mathrm{T}w'}}\right)\left(S_{\mathrm{ov},w'w}/\pi R_{w'w}^2\right)\right] \quad (33)$$

Assume that WT w' is upstream and WT w is downstream, and the intersection area is calculated as (34). Therefore, the number of WTs at the upstream part of WT w within the intersection area, G_{W}, can be determined as follows:

$$\begin{aligned} &S_{\mathrm{ov},w'w} = \\ &\arccos[(R_{w'w}^2+d^2-R^2)/2R_{w'w}d]\cdot R_{w'w}^2 \\ &\quad+\arccos[(R^2+d^2-R_{w'w}^2)/2Rd]\cdot R^2 \\ &\quad-\sin\{\arccos[(R_{w'w}^2+d^2-R^2)/2R_{w'w}d]\}R_{w'w}d \end{aligned} \quad (34)$$

Wind speed of WT w considering wake effect can be calculated by the following expression:

$$v_w = v_m\left[1-\sqrt{\sum_{w'=1}^{G_{\mathrm{W}}}(1-v_{w'w}/v_m)^2}\right] \quad (35)$$

According to natural wind speed each OWF, the actual input wind speed of each WT under the wake effect can be calculated using (32)–(35), and then $P_{wj\max}$ of each WT can be calculated using (31). Natural wind speed and $P_{wj\max}$ of each WT exhibit a one-to-one correspondence. Thus, uncertainties of offshore wind speeds in the model are equivalent to uncertainties of $P_{wj\max}$ of each WT. For the scenario-based risk-averse SED model, wind speeds of OWFs can be sampled first, and subsequently, the $P_{wj\max}$ of each WT can be calculated under each scenario. Therefore, in the optimization process of the proposed model, the nonlinear equations (31)–(35) are not included.

Therefore, the risk-averse SED model of a power system with multiple OWFs can be formulated as (7)–(9), (11)–(27), (29), (30). Because of variables of multiple stochastic scenarios, multiple periods, and multiple regional networks are included, the model size is large, and it is difficult to obtain optimal risk-averse decisions directly when applied in a large-scale power system. Thus, a distributed and risk-averse ADP algorithm is designed to solve the proposed risk-averse SED model.

IV. Solution Methodology

A. Centralized Risk-averse ADP Algorithm

For the aforementioned risk-averse SED model, if $R_{p,t}$, $R_{b,t}$ are deemed as storage quantities $\boldsymbol{R}_t$ and $v_{m,t}$ is deemed as exogenous uncertain variables $\boldsymbol{v}_t$, then the system state can be defined as $\boldsymbol{S}_t=(\boldsymbol{v}_t,\boldsymbol{R}_t)$, and the decision vector is expressed as $\boldsymbol{x}_t = (P_{g,t}, P_{\mathrm{pp},t}, P_{\mathrm{gp},t}, P_{\mathrm{cb},t}, P_{\mathrm{db},t}, P_{wj,t}, Q_{wj,t})$. State transition equations are shown in (14) and (20). Then the multi-period risk-averse SED model can be solved period by period using the ADP algorithm. Transformation of the multi-period risk-averse SED model into a series of deterministic single-period ED models and detailed solution steps of the algorithm are introduced below.

1) Transformation of the Multi-Period Model

The aforementioned risk-averse SED model can be transformed into deterministic optimization model by using the risk-averse ADP algorithm. According to the risk-averse Bellman recursion equation [33], the optimal solution of each period must be satisfied (36) when solving the multi-period risk-averse SED model with the objective function as (7), and instant cost at period t is (37).

$$V_t(\boldsymbol{S}_t)=\min_{\boldsymbol{x}_t\in\boldsymbol{\Pi}_t} C_t(\boldsymbol{S}_t,\boldsymbol{x}_t)+\rho_t^{\mathrm{risk}}(V_{t+1}(\boldsymbol{S}_{t+1})|\boldsymbol{S}_t) \quad (36)$$

$$\begin{aligned} C_t(\boldsymbol{S}_t,\boldsymbol{x}_t)=\sum_{g\in\Omega_{\mathrm{G}}}F_{g,t}+\sum_{m\in\Omega_{\mathrm{OWF}}}\sum_{w\in\Omega_m}C_{\mathrm{W}m}(P_{wj\max,t} \\ -P_{wj,t}) \end{aligned} \quad (37)$$

Expression of the risk-measurement term $\rho_t^{\mathrm{risk}}(V_{t+1}(\boldsymbol{S}_{t+1})|\boldsymbol{S}_t)$ is as (8). Here, $\rho_t^{\mathrm{risk}}(V_{t+1}(\boldsymbol{S}_{t+1})|\boldsymbol{S}_t)$ in the value function calculation includes mathematics expectation operation, which makes (36) difficult to obtain optimal risk-averse decision $\boldsymbol{x}_t$. Equation (36) can be simplified by introducing the pre-decision state $\boldsymbol{S}_t=(\boldsymbol{v}_t,\ \boldsymbol{R}_t)$ and post-decision state $\boldsymbol{S}_t^x=(\boldsymbol{v}_t,\boldsymbol{R}_t^x)$, state will transit from $\boldsymbol{S}_{t-1}^x$ to $\boldsymbol{S}_t$ after observing exogenous stochastic variables $\boldsymbol{v}_t$, and state will transit from $\boldsymbol{S}_t$ to $\boldsymbol{S}_t^x$ after executing decision variables $\boldsymbol{x}_t$. By observing $\boldsymbol{v}_t$ and executing $\boldsymbol{x}_t$ separately, value functions of pre-decision and post-decision states are written as (38) and(39), respectively [34].

$$V_t(\boldsymbol{v}_t,\boldsymbol{R}_t)=\min_{\boldsymbol{x}_t\in\psi_t}\left(C_t(\boldsymbol{v}_t,\boldsymbol{R}_t,\boldsymbol{x}_t)+V_t^x(\boldsymbol{v}_t,\boldsymbol{R}_t^x)\right) \quad (38)$$

$$V_t^x(\boldsymbol{v}_t,\boldsymbol{R}_t^x)=\rho_t^{\mathrm{risk}}(V_{t+1}(\boldsymbol{v}_{t+1},\boldsymbol{R}_{t+1})|(\boldsymbol{v}_t,\boldsymbol{R}_t^x)) \quad (39)$$

If the analytical expression of $V_t^x(\boldsymbol{v}_t,\boldsymbol{R}_t^x)$ is obtained, then (38) is a deterministic optimization model. Here, can be calculated by (39) with the risk-measurement term ρ_t^{risk} $(V_{t+1}(S_{t+1})|S_t)$, and obtaining exact $V_t^x(\boldsymbol{v}_t,\boldsymbol{R}_t^x)$ is difficult. As shown in (8), $V_t^x(\boldsymbol{v}_t,\boldsymbol{R}_t^x)$ is equal to the linear weighted sum of expected operation cost and GlueVaR measure, and the GlueVaR measure is convex given proper parameters of (k_1, k_2) as in Fig. 2. Hence, $V_t^x(\boldsymbol{v}_t,\boldsymbol{R}_t^x)$ is also convex. Thus, piecewise linear functions are applied to approximate value function $V_t^x(\boldsymbol{v}_t,\boldsymbol{R}_t^x)$ as follows [19]:

$$V_t^x(\boldsymbol{v}_t,\boldsymbol{R}_t^x)=\sum_{s\in N_{\mathrm{s}}}\theta_s(V_{ts,0}+\boldsymbol{k}_{ts}^{\mathrm{T}}\boldsymbol{\mu}_{ts}) \quad (40)$$

Therefore, (38) can be transformed into the following expression:

$$V_t(\boldsymbol{v}_t,\boldsymbol{R}_t)=\min_{\boldsymbol{x}_t\in\boldsymbol{\psi}_t}C_t(\boldsymbol{v}_t,\boldsymbol{R}_t,\boldsymbol{x}_t)+\sum_{s=1}^{N_{\mathrm{s}}}\theta_s(V_{ts,0}+\boldsymbol{k}_{ts}^{\mathrm{T}}\boldsymbol{\mu}_{ts}) \quad (41)$$

Thus, solving the multi-period risk-averse SED model is transformed into successively solving the single-period deterministic ED model as follows:

$$\begin{aligned} &\min_{\boldsymbol{x}_t\in\boldsymbol{\psi}_t}C_t(\boldsymbol{v}_t,\boldsymbol{R}_t,\boldsymbol{x}_t)+\sum_{s\in N_{\mathrm{s}}}\theta_s(V_{ts,0}+\sum_{r\in B_s}k_{ts,r}\mu_{ts,r}) \\ &\text{s.t.}\quad (9),\ (11)\text{–}(27),\ (29),\ (30) \\ &\sum_{r\in B_s}\mu_{ts,r}=R_{s,t}^x,\mu_{ts,r}\in[0,R_{s,\max}/B_s],s\in N_{\mathrm{ps}} \end{aligned} \quad (42)$$

2) Algorithm Steps

Similar to the conventional ADP algorithm, to obtain piecewise linear risk-averse AVFs, the risk-averse ADP algorithm also requires sufficient scenarios to train and correct slopes and intercepts of the risk-averse AVFs. After obtaining trained risk-averse AVFs, substitute these values into (42) to obtain risk-averse decisions by successively solving the single-period deterministic ED model (42) under the forecast scenario. The specific steps of the risk-averse ADP algorithm are as follows:

a) Initialization: Solve the deterministic ED model under the forecast scenario, and obtain the operation cost of each period. Next, the initial value of the AVF of post-decision state at period t should be the sum of the operation costs from period $t+$ 1 to the final period T as follows:

$$V_t^0 = \sum_{t'=t+1}^{T} C_{t'(\boldsymbol{S}_{t'},\boldsymbol{x}_{t'})} \tag{43}$$

Storage quantities of the deterministic ED solution are used as optimal storage quantity of each storage at each period $\boldsymbol{R}_t^{x0}$. Initial slope $\boldsymbol{k}_{ts,0}$ can be given as in [19], and then initial intercept $V_{ts,0}$ can be obtained using the following expression:

$$V_{ts,0} = V_t^0 - \boldsymbol{k}_{ts0}^{\mathrm{T}} \boldsymbol{u}_{ts} \tag{44}$$

b) Training of risk-averse AVFs: Based on the forecast scenario of natural wind speeds $\boldsymbol{v}^0 = (\boldsymbol{v}_1^0, \cdots, \boldsymbol{v}_T^0)$, N error scenarios $\boldsymbol{v}^n = (\boldsymbol{v}_1^n, \cdots, \boldsymbol{v}_T^n)$, $n = 1 \sim N$ are generated by the Monte-Carlo sampling method. Sampling scenarios are randomly divided into G groups, and each group contains $num = N/G$ scenarios. Next, (42) is solved by successive periods under each scenario in one group to obtain operation cost of each scenario. Cumulative distribution function (CDF) of the operation cost can be obtained from equal probability value and operation cost of each scenario in the group.

However, because of the limited number of scenarios in each group, the obtained CDF of operation cost is discrete. Here, the piecewise linear interpolation method is used to calculate approximate risk-measurement cost, that is, risk-averse AVFs. For the sc-th group of scenarios, assume the vector $\bar{\boldsymbol{V}}_t$ is composited of total operation cost from $t+1$ period to final period T of each scenario, that is, $\bar{\boldsymbol{V}}_t = [\overline{V}_t^1, \overline{V}_t^2, \cdots, \overline{V}_t^{\mathrm{num}}]$ and $\overline{V}_t^1 < \overline{V}_t^2 < \cdots < \overline{V}_t^{\mathrm{num}}$. Next, expectation and cumulative probability values can be approximated and calculated as follows:

$$E(\overline{V}_t) = \sum_{i=1}^{\mathrm{num}} \overline{V}_t^i / num \tag{45}$$

$$\varphi(\overline{V}_t^i) = P(X \le \overline{V}_t^i) = i/num,\ i = 1, 2, \cdots, num \tag{46}$$

Next, the discrete inverse function of the CDF can be obtained as follows:

$$\varphi^{-1}(P(X \le \overline{V}_t^i)) = \overline{V}_t^i,\ i = 1, 2, \cdots, num \tag{47}$$

Based on the aforementioned discrete inverse function, the continuous function $\varphi^{-1}(\cdot)$ can be obtained by the piecewise linear interpolation method. Hence, VaR_α, CVaR_α and CVaR_β, and $\mathrm{GlueVaR}_{\beta,\alpha}^{k_1,k_2}$ in (48)(51) can be calculated. The latest risk-averse AVFs $\tilde{V}_t^{sc}$ can be obtained from (52). Based on $\bar{\boldsymbol{V}}_t^i$ and $R_t^{x,i}$, $i = 1, 2, \cdots, num$. The discrete corresponding relationship between $\bar{\boldsymbol{V}}_t^i$ and $R_t^{x,i}$ can be obtained. Next, the optimal storage quantity $R_t^{x,sc}$ corresponding to $\tilde{V}_t^{sc}$ can be obtained by using the piecewise linear interpolation method. Slopes and intercepts of the risk-averse AVFs are updated by the successive projection approximation routine algorithm [32], and risk-averse AVFs gradually approach accurate $\rho_t^{\mathrm{risk}}(\boldsymbol{v}_t, \boldsymbol{R}_t^x)$. When risk-averse AVFs of the two adjacent iterations are close in all periods, iteration process converges.

$$\mathrm{VaR}_\alpha(\overline{V}_t) = \varphi^{-1}(\alpha) \tag{48}$$

$$\mathrm{CVaR}_\alpha(\overline{V}_t) = \int_\alpha^1 \varphi^{-1}(u)\mathrm{d}u/(1-\alpha) \tag{49}$$

$$\mathrm{CVaR}_\beta(\overline{V}_t) = \int_\beta^1 \varphi^{-1}(u)\mathrm{d}u/(1-\beta) \tag{50}$$

$$\begin{aligned}\kappa_{\beta,\alpha}^{k_1,k_2}(\overline{V}_t) &= k_1 \mathrm{CVaR}_\beta(\overline{V}_t) + k_2 \mathrm{CVaR}_\alpha(\overline{V}_t) \\ &\quad + k_3 \mathrm{VaR}_\alpha(\overline{V}_t)\end{aligned} \tag{51}$$

$$\tilde{V}_t^{sc} = (1-\lambda)E(\overline{V}_t) + \lambda \kappa_{\beta,\alpha}^{k_1,k_2}(\overline{V}_t) \tag{52}$$

B. Distributed and Risk-averse ADP Algorithm Based on ADMM

The aforementioned centralized single-period deterministic ED model of a power system with multiple OWFs as (42) is a convex programming model, which can be solved in a fully distributed manner by using the synchronous ADMM algorithm [35]. For a typical two-region optimization problem as (53), the augmented Lagrangian functions of each region in the k-th iteration can be expressed as follows:

$$\begin{aligned}&\min_{\boldsymbol{x}_1,\boldsymbol{x}_2} c_1(\boldsymbol{x}_1) + c_2(\boldsymbol{x}_2) \\ &\text{s.t.} \begin{cases} \boldsymbol{x}_1 \in \psi_{1t}, & \boldsymbol{x}_2 \in \psi_{2t} \\ x_{1,\mathrm{bc}} = x_{2,\mathrm{bc}} \end{cases}\end{aligned} \tag{53}$$

$$\begin{aligned}L_1(\boldsymbol{x}_1, z_1^k, \lambda_1^k) &= c_1(\boldsymbol{x}_1) + \lambda_1^k(x_{1,\mathrm{bc}} - z_1^k) \\ &\quad + (\rho/2)\|x_{1,bc} - z_1^k\|_2^2\end{aligned} \tag{54}$$

$$\begin{aligned}L_2(\boldsymbol{x}_2, z_2^k, \lambda_2^k) &= c_2(\boldsymbol{x}_2) + \lambda_2^k(x_{2,\mathrm{bc}} - z_2^k) \\ &\quad + (\rho/2)\|x_{2,bc} - z_2^k\|_2^2\end{aligned} \tag{55}$$

where the intermediate variables $z_1^k = z_2^k = (x_{1,\mathrm{bc}} + x_{2,\mathrm{bc}})/2$.

The update process of $\boldsymbol{x}_1$, $\boldsymbol{x}_2$, λ_1, and λ_2 in the synchronous ADMM algorithm are as (56)–(58). When convergence criterion given by (59) is satisfied, the iteration process terminates and the solution is obtained.

$$\begin{cases} \boldsymbol{x}_1^{k+1} = \mathrm{argmin} L_1(\boldsymbol{x}_1, z_1^k, \lambda_1^k) \\ \boldsymbol{x}_2^{k+1} = \mathrm{argmin} L_2(\boldsymbol{x}_2, z_2^k, \lambda_2^k) \end{cases} \tag{56}$$

$$z_1^{k+1} = z_2^{k+1} = (x_{1,\mathrm{bc}}^{k+1} + x_{2,\mathrm{bc}}^{k+1})/2 \tag{57}$$

$$\begin{cases} \lambda_1^{k+1} = \lambda_1^k + \rho(x_{1,\mathrm{bc}}^{k+1} - z_1^{k+1}) \\ \lambda_2^{k+1} = \lambda_2^k + \rho(x_{2,\mathrm{bc}}^{k+1} - z_2^{k+1}) \end{cases} \tag{58}$$

$$\begin{cases} \Delta_{\mathrm{p}} = \|x_{1,\mathrm{bc}}^{k+1} - x_{2,\mathrm{bc}}^{k+1}\|_2 \le \varepsilon_1 \\ \Delta_{\mathrm{d}} = \|x_{2,\mathrm{bc}}^{k+1} - x_{2,\mathrm{bc}}^{k}\|_2 \le \varepsilon_2 \end{cases} \tag{59}$$

where Δ_{p} and Δ_{d} are primal residual and dual residual at the $(k+1)$-th iteration, respectively.

Assume m-th OWF is connected to the transmission system through connection bus c_m. Bus tearing method is used to

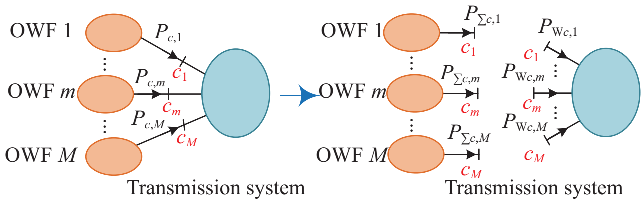

Fig. 3. Decoupling by the bus tearing method.

devolve the OWF and transmission system, as displayed in Fig. 3. Next, active power across connection bus c_m is equivalent to the injected power of bus c_m into transmission system $P_{\mathrm{W}c,m}$ and total active power output of the OWF into bus cm $P_{\Sigma cm}$. Thus, $P_{\mathrm{W}c,m}$ and $P_{\Sigma c,m}$ can be defined as boundary coupling variables, with boundary coupling constraint as(60) to ensure consensus of the distributed solution of transmission system and the m-th OWF.

$$P_{\mathrm{W}c,m,t} = P_{\Sigma c,m,t} \tag{60}$$

Because instant cost and AVFs in (42) are separable between the transmission system and each OWF, in the distributed solution of the single-period deterministic ED model, the subproblems of transmission network and m-th OWF at K-th iteration can be defined as follows:

$$\begin{aligned}
&\min\Bigg\{\sum_{g\in\Omega_{\mathrm{G}}} F_{g,t} + \sum_{p\in N_{\mathrm{ps}}} \theta_p(V_{tps,0} + \sum_{r\in B_p} k_{tp,r}\mu_{tp,r}) \\
&\quad + \sum_{m\in\Omega_{\mathrm{OWF}}} [\lambda_{1,m}^K (P_{\mathrm{W}c,m,t} - z_{c,m,t}^K) \\
&\quad + \rho/2\|P_{\mathrm{W}c,m,t} - z_{c,m,t}^K\|_2^2]\Bigg\} \\
&\text{s.t.}\quad (11)\text{–}(19) \\
&\quad \sum_{r\in B_p} \mu_{tp,r} = R_{p,t}^x, \mu_{tp,r} \in [0, R_{p,\max}/B_p],\ \ p\in N_{\mathrm{ps}}
\end{aligned} \tag{61}$$

$$\begin{aligned}
&\min\Bigg\{\sum_{w\in\Omega_m} C_{\mathrm{W}m}(P_{wj\max,t} - P_{wj,t}) \\
&\quad + \sum_{b\in N_{\mathrm{bs},m}} \theta_b\Bigg(V_{tbs,0} + \sum_{r\in B_b} k_{tb,r}\mu_{tb,r}\Bigg) \\
&\quad + \lambda_{2,m}^K (P_{\Sigma c,m,t} - z_{c,m,t}^K) + \rho/2\|P_{\Sigma c,m,t} - z_{c,m,t}^K\|_2^2\Bigg\} \\
&\text{s.t.}\quad (20)\text{–}(27),\ (29),\ (30) \\
&\quad \sum_{r\in B_b} \mu_{tb,r} = R_{b,t}^x, \mu_{tb,r} \in [0, R_{b,\max}/B_b],\ \ b\in N_{\mathrm{bs},m}
\end{aligned} \tag{62}$$

The synchronous ADMM algorithm is embedded into the risk-averse ADP algorithm in the AVF training process, and the optimal solution obtaining process to realize the distributed solution and maintain information privacy between transmission system and multiple OWFs. Flowchart of the distributed and risk-averse ADP (DRADP) algorithm is displayed in Fig. 4.

V. Case Studies

Case studies are conducted on a modified IEEE 39-bus system with an OWF and an actual provincial power system with four OWFs. Parameters of the GlueVaR risk-measurement are set as $\alpha = 0.8$, $\beta = 0.95$, $k_1 = 0.4$, $k_2 = 0.3$. Assume predicted errors of wind speeds obey normal distribution with $(\mu, \sigma^2) = (0, 0.15^2)$, while largest deviation should be less than 30% of predicted wind speed. Based on the forecast scenario, 200 sampling scenarios are generated by Monte-Carlo method, which are randomly divided into 20 groups (10 scenarios in each group) for training risk-averse AVFs. Thresholds of ADMM algorithm are set as $\varepsilon_1 = \varepsilon_2 = 10^{-3}$. Computing platforms are GAMS 24.5 and MATLAB 2017a, and the GUROBI solver in GAMS is used to solve optimization models (61) and (62). Parallel computation was conducted using a blade cluster composed of 24 HPE BL460C GEN10 computing blades, where each computing blade was composed of two 2.30 GHz Intel Gen10 Xeon-G 5118 (12 cores) processors and 128 GB of RAM.

A. Modified IEEE 39-bus System with an OWF

1) System Parameters

The modified IEEE 39-bus system includes a PSH station and an OWF connected with a BS station as displayed in Fig. 5. Number of WTs in the OWF is 91. The rated power of each WT is 8 MW, whereas the minimum power output is 0.103 MW. The cut-in wind speed, rated wind speed, and cut-out wind speed were 3, 13, and 25 m/s, respectively. Parameters of PSH and BS stations are $R_{p,0} = 1000$ MWh, $R_{p,\max} = 2000$ MWh, $P_{\mathrm{pp},\max} = P_{\mathrm{gp},\max} = 400$ MW, $R_{b,0} = 70$ MWh, $R_{b,\max} = 140$ MWh, and $P_{\mathrm{cb},\max} = P_{\mathrm{db},\max} = 30$ MW. Total active load curve of the system is displayed in Fig. 6. Forecast and sampling scenarios of wind speed are shown in Fig. 7.

2) Analysis of AVF Training and Solution Results

Changes in risk-averse AVFs of each period during training of first and last five groups of scenarios are displayed in Fig. 8. With increase in number of training scenario groups, risk-averse AVFs of each period gradually converge, which reveals excellent convergence of the proposed algorithm for training risk-averse AVFs.

Solution results of different algorithms, including the proposed DRADP and CRADP algorithms, RO algorithm, and scenario-based SO algorithm, are listed in Table I. Among them, the same sampling scenarios of the proposed DRADP algorithm are used in the scenario-based SO algorithm, and maximum and minimum wind speeds in sampling scenarios are taken as upper and lower bounds of uncertainty sets in the RO algorithm. Table I shows that the results of RO algorithm are conservative, and the total operation cost is bigger, while results of scenario-based SO algorithm are optimistic, and total operation cost is smaller. However, scenario-based SO algorithm consumes much more time than the proposed DRADP and CRADP algorithms. Total operation cost obtained by the two proposed algorithms is close, which indicates distributed optimization in the DRADP algorithm does not affect optimality of decision-making. For CPU time because scale of the single-period ED model after decoupling is small, the DRADP algorithm requires multiple distributed iterations

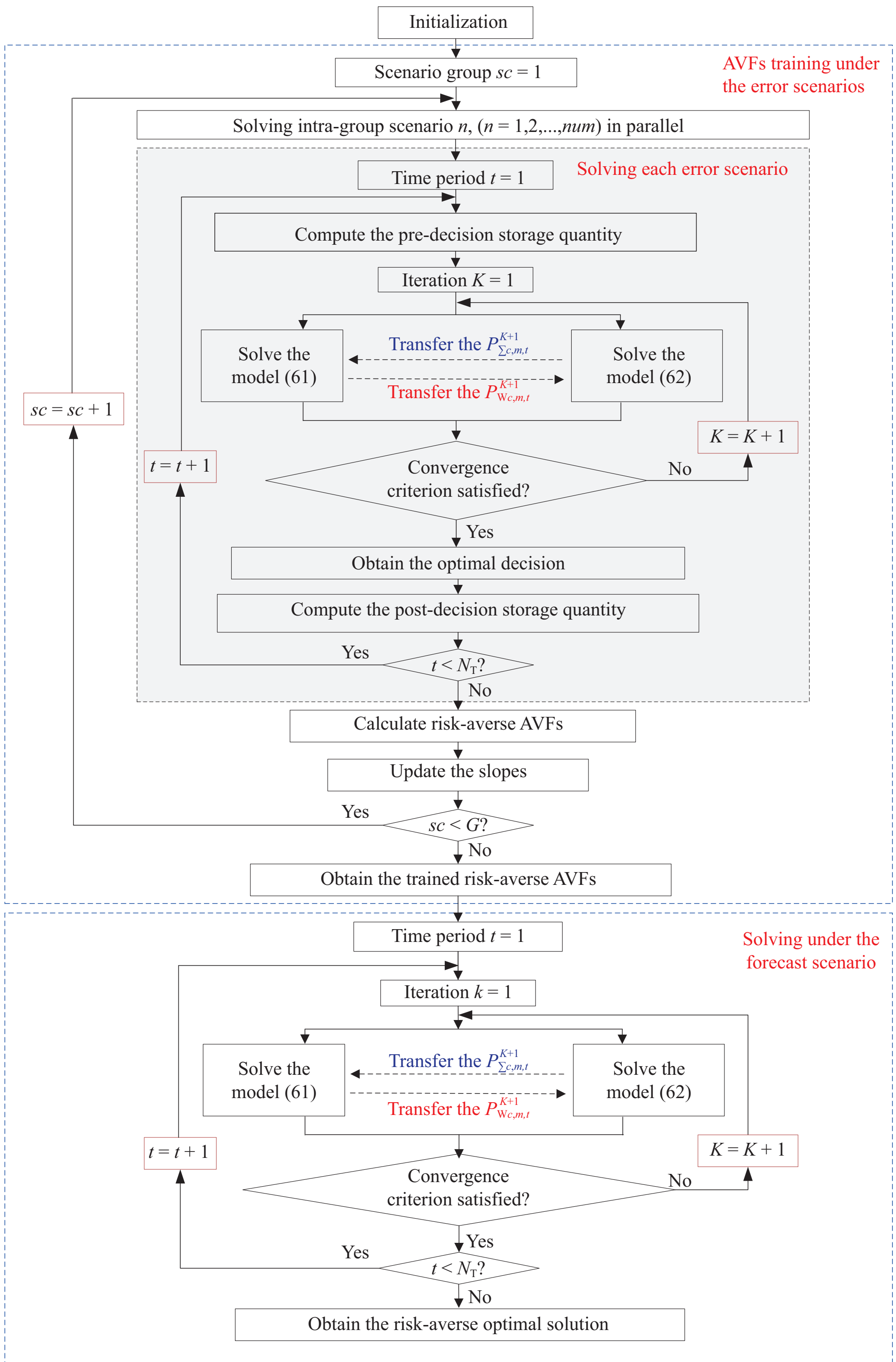

Fig. 4. Flowchart of the distributed and risk-averse ADP algorithm.

and consumes more CUP time than the CRADP algorithm. But the DRADP algorithm only needs to transmit a small amount of boundary connection bus information of adjacent regions during the calculation process, which can maintain the information privacy of the transmission system and the OWF.

The total number of sampling scenarios remains unchanged, and comparative results with different G values in the AVF training process of the DRADP algorithm are shown in Table II. It can be seen with the increase of G values, total operation costs slightly decrease, but consumed total CPU time increases greatly. Increasing G values means increasing the number of groups and decreasing the number of scenarios per group. Increasing groups results in more training time because risk-averse AVFs are trained group by group and decreasing scenarios per group results in the lack of covering scenarios in high-risk regions and low-risk aversion degrees. In

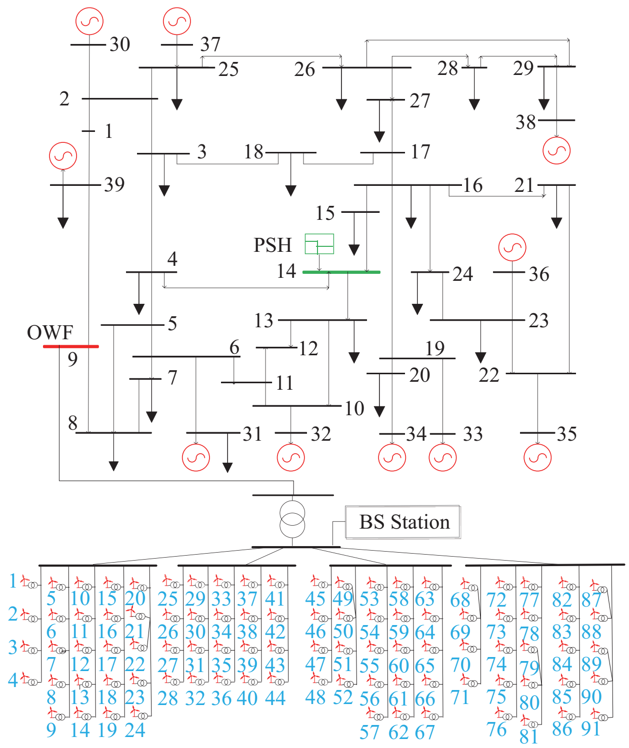

Fig. 5. Topology of the modified IEEE 39-bus system with an OWF.

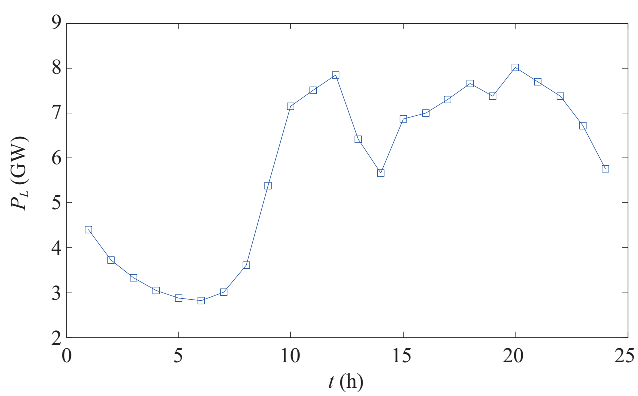

Fig. 6. Total active load curve.

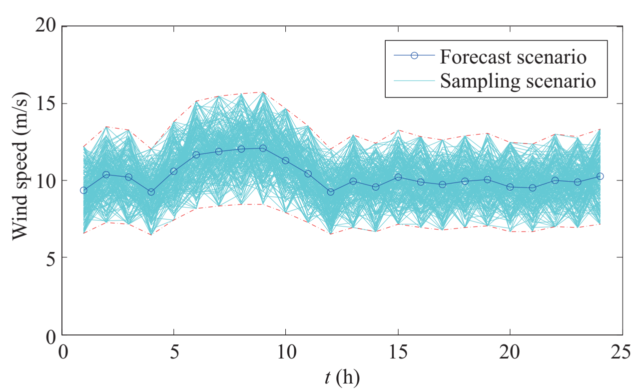

Fig. 7. Forecast and sampling scenarios of the wind speed.

addition, change curves of Δ_p and Δ_d at all periods with the number of distributed iterations, and the required total number

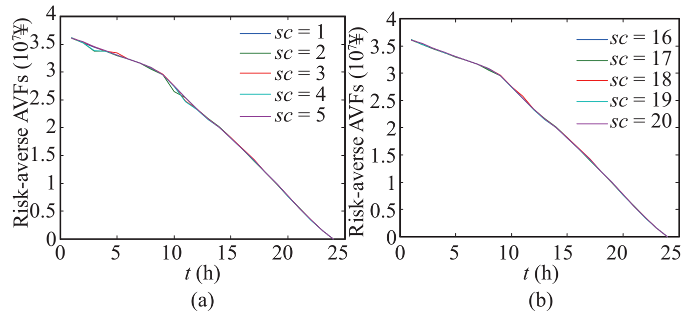

Fig. 8. Changes in the risk-averse AVFs of each period during the training. (a) First five groups of scenarios. (b) Last five groups of scenarios.

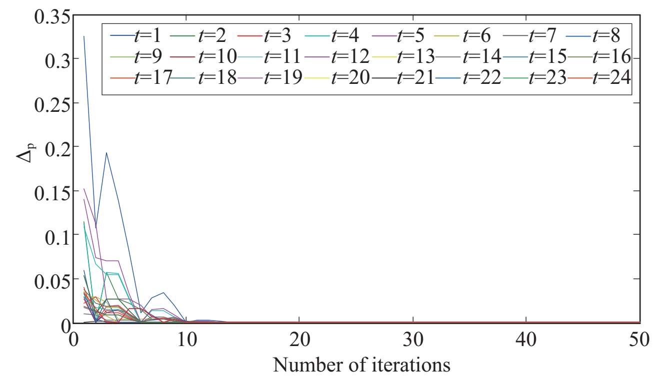

Fig. 9. Change curves of Δ_p at all the periods.

TABLE I
COMPARATIVE SOLUTION RESULTS OF DIFFERENT ALGORITHMS

Algorithm	Total operation cost (¥)	Training time (s)		Decision time (s)
		Serial computing	Parallel computing	
CRADP	37 113008.8	2 970.5	326.8	6.8
DRADP	37 113020.1	8 863.6	421.3	21.8
RO	37 299453.2	–	–	268.4
Scenario-based SO	37 104789.6	–	–	8 941.5

TABLE II
COMPARATIVE RESULTS OF DRADP ALGORITHM WITH DIFFERENT G VALUES

G	num	Total operation cost (¥)	Training time (s)	Decision time (s)	Total time (s)
10	20	37 114654.2	235.5	20.9	256.4
20	10	37 113020.1	421.3	21.8	443.1
40	5	37 110478.4	945.7	22.2	967.9

of iterations at each period are displayed in Figs. 9–11. The distributed optimization computation of the proposed DRADP algorithm exhibits an excellent convergence performance. In some periods, such as periods 17–21, the total number of iterations in these periods was reduced considerably because solution of the previous period can provide excellent initial values for distributed optimization computation.

In the obtained risk-averse SED scheme, changes in storage quantities and active power output of PSH and BS stations are displayed in Fig. 12. Storage units charge power or pump water when the active load of the system is low, and discharge power or generate power when the active load is high, which plays a role in shaving peak load in system operation. Therefore,

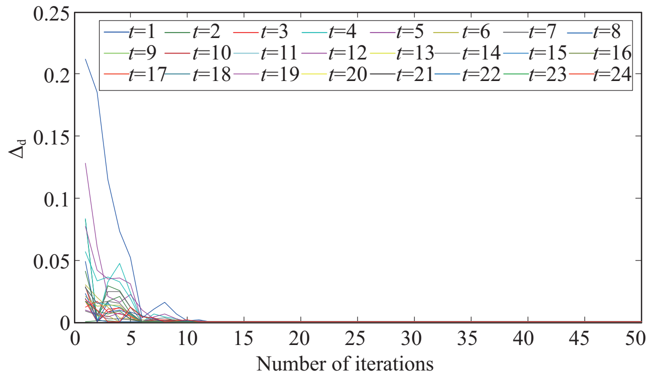

Fig. 10. Change curves of $\Delta_{\rm d}$ at all the periods.

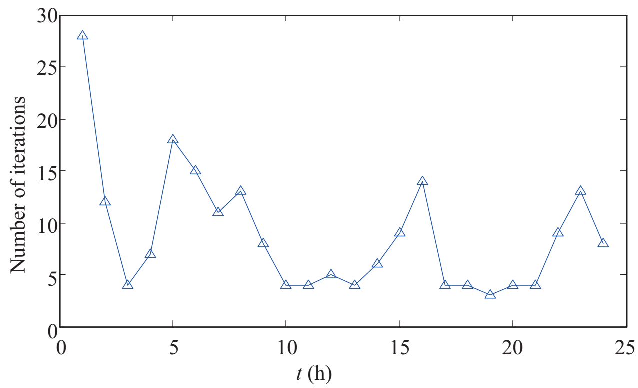

Fig. 11. Required total number of iterations at each period.

thermal power units can be operated economically to reduce total operation costs. The active power output of OWF and the total maximum available active power output of WTs are displayed in Fig. 13. During periods 5–9, OWF reduces active power output to charge power into the BS station. In contrast BS station discharges power during periods 12 and 20. This process reduces the volatility of the total active power output of the OWF. Thus, the BS station plays a crucial role in absorbing excess wind power at high wind speed periods to reduce the amount of wind curtailment.

3) Comparison of the Decision Results Under Various Risk-Measurement Parameters

In the proposed DRADP algorithm, various risk-measurement parameter values affect the conservatism of decision results. Given confidence levels $\alpha = 0.8$, $\beta = 0.95$, value range of (k_1, k_2) can be obtained as displayed in Fig. 14. Various parameter combinations are considered within the value range in Fig. 14, and values of obtained total operation costs are normalized in interval [37 110000, 37 116000], as displayed in Fig. 15. These results revealed the conservatism of decision results can be adjusted flexibly by changing the combination of (k_1, k_2) under given confidence levels, and the closer the value of (k_1, k_2) is to (0.25, 0), the more economical decision results are; the closer the value of (k_1, k_2) is to (1, 0), the more conservative the decision results are.

Assuming predicted errors of wind speeds obey $N(0, 0.15^2)$, 100 new sampling scenarios are generated and used to demonstrate the performance of risk-averse decisions under various (k_1, k_2) values. A comparison of decision results for various (k_1, k_2) values is presented in Table III. When values of (k_1, k_2) are (0.0, 1.0) and (1.0, 0.0), GlueVaR is equal to CVaR_α, i.e., $\mathrm{CVaR}_{0.80}$, and CVaR_β, i.e., $\mathrm{CVaR}_{0.95}$, respectively. It can be seen that given confidence levels $\alpha = 0.8$, $\beta = 0.95$, GlueVaR risk-measurement can cover $\mathrm{CVaR}_{0.80}$ and $\mathrm{CVaR}_{0.95}$ by properly adjusting parameters. GlueVaR risk-measurement method can also obtain risk aversion degree between $\mathrm{CVaR}_{0.80}$ and $\mathrm{CVaR}_{0.95}$, which indicates GlueVaR risk-measurement method is more flexible than CVaR risk-measurement method. When values of (k_1, k_2) are closer to (1.0, 0.0), decision results are more conservative, and the operation cost of forecast scenario and the average operation cost of sampling scenarios are higher, but risk-measurement GlueVaR cost is lower. Therefore, in practice, parameters (k_1, k_2) can be flexibly selected to satisfy various risk requirements of power system operation.

TABLE III
COMPARISON OF DECISION RESULTS FOR VARIOUS PARAMETER VALUES

Value of (k_1, k_2)	Operation cost of forecast scenario (¥)	Average operation cost (¥)	GlueVaR cost (¥)	(GlueVaR - average operation cost) (¥)
Risk-neutral	37 105648.7	37 111433.3	37 370121.9	258688.6
(0.25, 0)	37 110789.5	37 117380.5	37 356168.3	238787.8
(0.0, 1.0)	37 112541.1	37 119523.3	37 348469.7	228946.4
(0.4, 0.3)	37 113020.1	37 120104.8	37 345485.6	225380.8
(1.0, 0.0)	37 115034.8	37 123159.8	37 329657.6	206497.8

4) Comparison of the Decision Results of Various Algorithms

In the conventional ADP algorithm, the risk cost of extreme scenarios in the AVF training process is not considered, and its decision-making is economical and risk-neutral. In the proposed DRADP algorithm, GlueVaR is used to consider the risk costs of extreme wind speed scenarios in the AVF training process, and the decision results are conservative. However, decision results are risk-averse. Comparative results of various algorithms are presented in Table IV. Among them, the optimal offline solution minimizes total cost with perfect information of uncertainties available in advance [34]. Although the operation cost of forecast scenario and the average operation cost of the proposed DRADP algorithm are higher than of the conventional ADP algorithm and the optimal offline solution, GlueVaR cost of the proposed DRADP algorithm is considerably lower than that of conventional ADP algorithm and is closer to the optimal offline solution, which indicates although the proposed DRADP algorithm sacrifices the economy of forecast scenario, it can reduce risk cost of

TABLE IV
COMPARATIVE RESULTS OF VARIOUS ALGORITHMS

Algorithm	Operation cost of forecast scenario (¥)	Average cost (¥)	GlueVaR cost (¥)	(GlueVaR-Average cost) (¥)
DRADP	37 113020.1	37 120104.8	37 345485.6	225380.8
Conventional ADP	37 105963.0	37 111841.7	37 369865.2	258023.5
Optimal offline solution	37 081545.3	37 104523.9	37 309072.3	204548.4

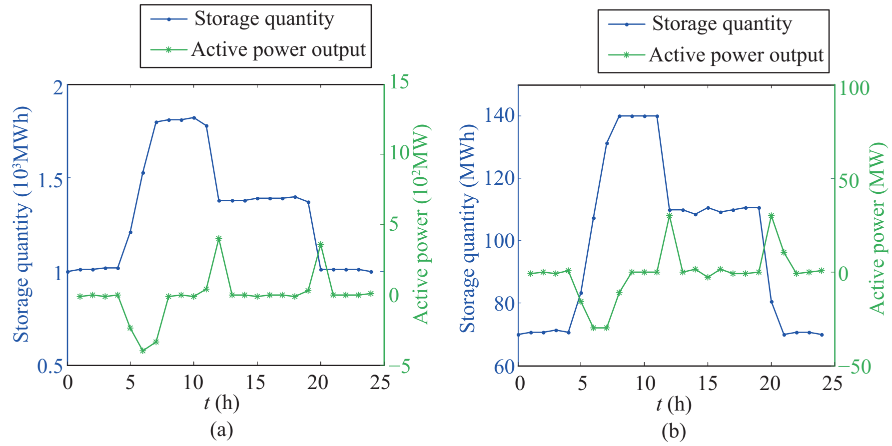

Fig. 12. Changes of storage quantities and active output of storage units. (a) PSH station. (b) BS station.

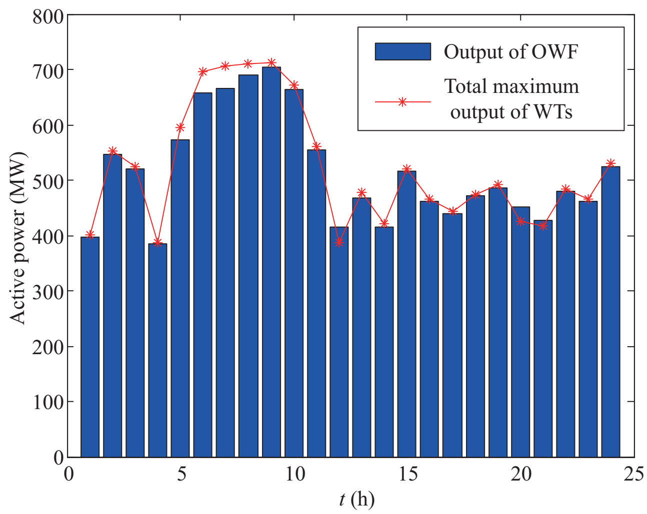

Fig. 13. Active power output of OWF and total maximum available power output of WTs.

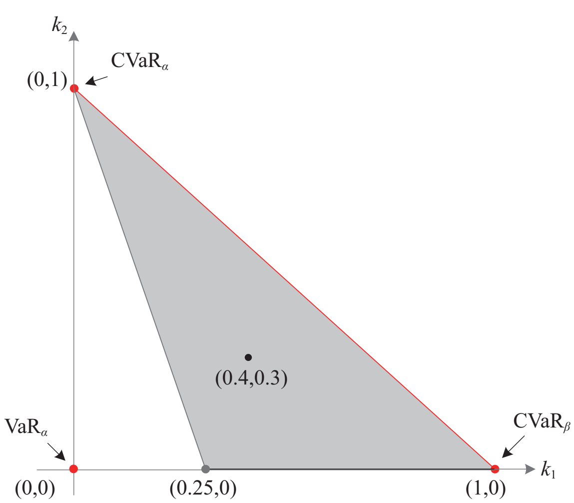

Fig. 14. Given α and β, the value range of (k_1, k_2).

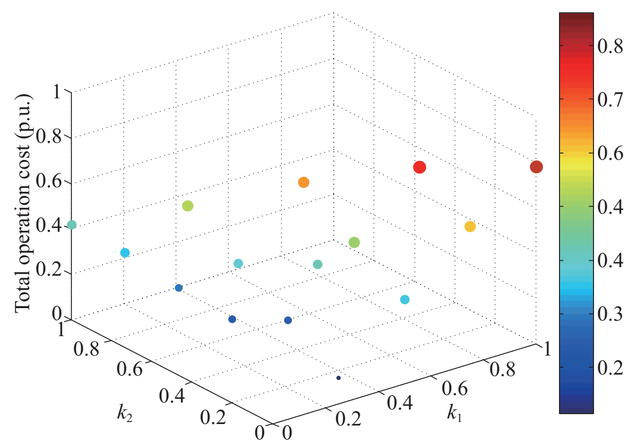

Fig. 15. Total operation cost of forecast scenario corresponding to various parameter combinations.

extreme scenarios and mitigates change range of operation costs under wind power fluctuation. In addition, the results of the conventional ADP algorithm are close to those of the risk-neutral DRADP algorithm in Table III, which reveals the decision of the conventional ADP algorithm is risk-neutral.

Comparison of the solution time of conventional ADP and DRADP algorithm is displayed in Table V. It can be found in the DRADP algorithm, multiple scenarios within the same group can be calculated in parallel computing in AVF training, while the conventional ADP algorithm can only solve multiple scenarios one by one in series computing in AVF training, hence consumed CPU time of the proposed DRADP algorithm is much smaller than of conventional ADP algorithm.

TABLE V
COMPARISON OF THE SOLUTION TIME OF VARIOUS ALGORITHMS

Algorithm	Training time (s)	Decision time (s)	Total CPU time (s)
DRADP	421.3	21.8	443.1
Conventional ADP	2 508.72	6.8	2 515.5

B. Actual Provincial Power System

The transmission system of the actual provincial power system has 2752 buses and 3003 branches, including 178 thermal power units (122 coal-fired units and 56 gas-fired units), 9 nuclear power units, 10 hydroelectric units, and 4 PSH stations. Four OWFs are connected to the transmission system.

Each OWF is equipped with a BS station at the offshore step-up substation. The topology of the 500-kV main network of the system with four OWFs is displayed in Fig. 16. Parameters of PSH stations and BS stations, total active load curve, forecast scenario of wind speed in each OWF, and topology of each OWF are presented in Appendix A.

Comparison of solution results of the DRADP, CRADP, and conventional ADP algorithms is presented in Table VI. Total operation costs of the DRADP and CRADP decisions are close, and their total operation costs are higher than conventional ADP decisions because of consideration of operation cost risk of extreme scenarios during AVF training. For CPU time, both DRADP and CRADP have less training time and total CPU time than conventional ADP, since multiple scenarios within the same group can be calculated in parallel computing in the AVF training process of the DRADP and CRADP algorithms. After the time period is decoupled, the scale of the single-period ED problem is small. The total CPU time of DRADP is more than CRADP because distributed computing requires multiple iterations, but they are very close. However, when more OWFs are integrated into the power system, the total CPU time of DRADP will be smaller than CRADP. Moreover, the DRADP algorithm only exchanges information on boundary variables between transmission system and multiple OWFs and maintains their information privacy. In this method, data confidentiality is realized between various stakeholders, which exhibits the incomparable advantages of the CRADP algorithm.

TABLE VI
COMPARATIVE RESULTS OF VARIOUS OPTIMIZATION ALGORITHMS

Algorithm	Total operation cost (10^4¥)	Training time (s)	Decision time (s)	Total CPU time (s)
DRADP	36 452.93	3 809.6	60.46	3 870.1
CRADP	36 450.66	3 435.1	52.11	3 487.2
Conventional ADP	36 388.84	31 806.2	51.42	31 857.6

Comparison of changes in storage quantities of storage units for the DRADP and ADP decisions is displayed in Fig. 17. Combined with the active load curve of the system as Fig. A1 in Appendix A, it can be seen storage units charge power or pump water when active load of the system is low, such as time periods 0–8 h, and discharge power or generate power when active load is high, such as time periods 11–13 h and 19–22 h. Changes in storage quantities show the positive effect of storage units in shaving peak load in system operation. Meanwhile, storage quantities of the DRADP decision tend to reserve more storage quantities than conventional ADP decisions to address extreme scenarios of a sudden drop in power output of OWFs at time periods of high active load. The difference in storage quantities between the DRADP and conventional ADP decisions also infers DRADP decisions are risk-averse while conventional ADP decisions are risk-neutral. Besides, thermal units in the forecast scenario do not operate in the most economical state, and the total operation cost of DRADP decisions is higher than conventional ADP decisions.

Solution results of the DRADP algorithm under various risk-measurement parameters of GlueVaR are compared in Table VII. When values of (k_1, k_2) are (0.0, 1.0) and (1.0, 0.0), GlueVaR is equal to CVaR_α, i.e., $\mathrm{CVaR}_{0.80}$, and CVaR_β, i.e., $\mathrm{CVaR}_{0.95}$, respectively. Risk preference of decision-making can be adjusted by appropriate adjustment of parameters in GlueVaR. When the risk measure is conservative, the average total operation cost is high, but it can reduce GlueVaR cost value in sampling scenarios and consequently reduce the variation range of total operation costs. When the risk measure is close to risk-neutral, decision results are economical. Therefore, decision-makers can flexibly select proper risk measures between conservatism and risk neutrality.

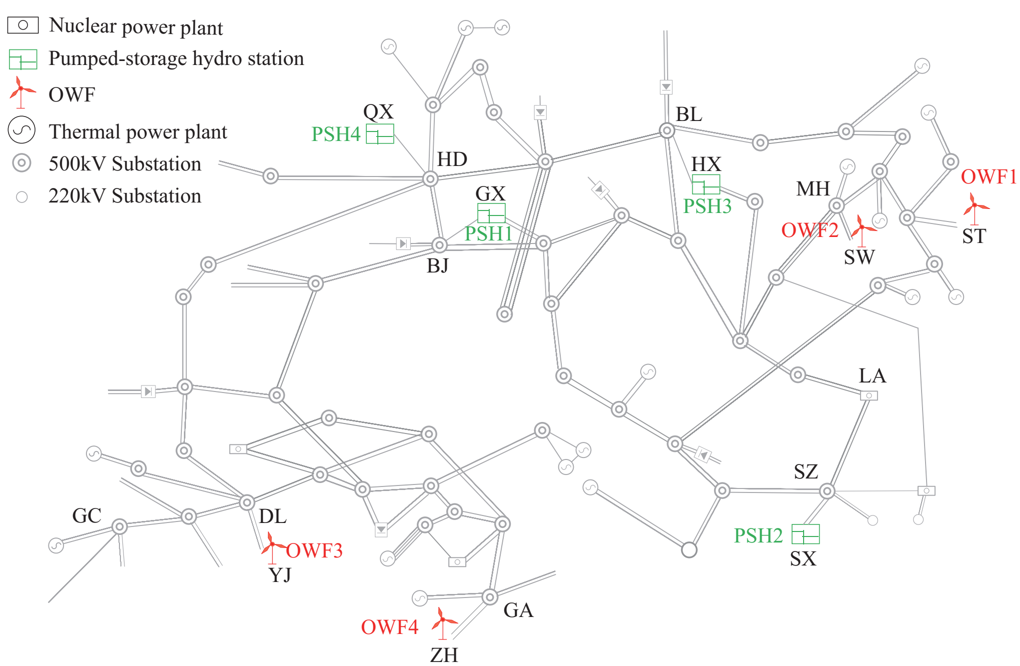

Fig. 16. Topology of 500-kV main network for the provincial power grid.

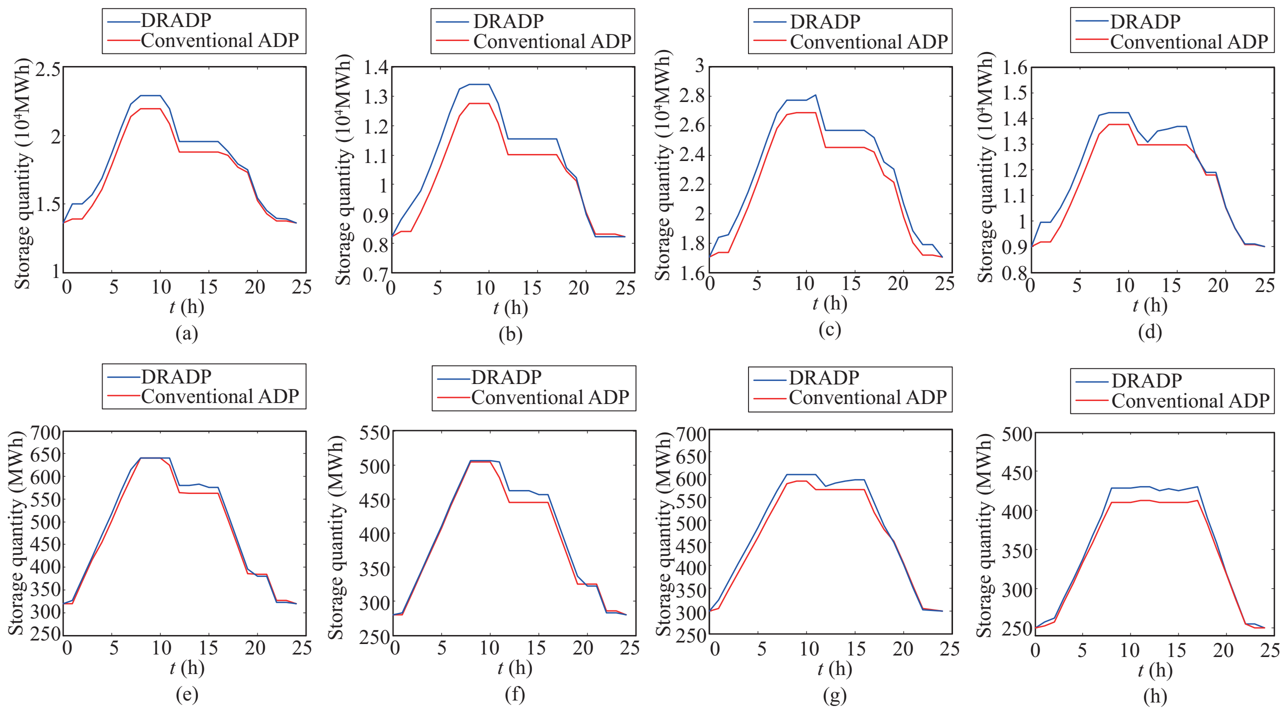

Fig. 17. Changes in the storage quantity of each storage unit for the DRADP and ADP algorithms. (a) PSH1. (b) PSH2. (c) PSH3. (d) PSH4. (e) BS of OWF1. (f) BS of OWF2. (g) BS of OWF3. (h) BS of OWF4.

TABLE VII
COMPARISON OF DECISION RESULTS FOR VARIOUS PARAMETER VALUES

Value of (k_1, k_2)	Operation cost of forecast scenario (10^4¥)	Average operation cost of error scenarios (10^4¥)	GlueVaR cost (10^4¥)	(GlueVaR - average operation cost) (10^4¥)
Risk-neutral	36 379.14	36 583.02	37 316.91	733.89
(0.25, 0)	36 420.29	36 617.57	37 241.73	624.16
(0.0, 1.0)	36 448.78	36 645.47	37 220.45	574.98
(0.4, 0.3)	36 452.93	36 653.10	37 218.74	565.64
(1.0, 0.0)	36 481.66	36 707.63	37 209.04	501.41

VI. CONCLUSION

This paper considers risk costs caused by random fluctuation of offshore wind speeds, and proposes a DRADP algorithm for SED of power system with multiple OWFs. The risk-aversion process is constructed by GlueVaR risk-measurement method, and distributed computing between transmission network and multiple OWFs is executed by introducing the ADMM algorithm into the risk-averse ADP algorithm. Case studies on the modified IEEE 39-bus system with an OWF and an actual provincial power system with four OWFs demonstrate the proposed DRADP algorithm can avoid risks of high operation costs caused by random fluctuation of offshore wind speeds. The operation cost of extreme scenarios is lower than that of risk-neutral decision results. By adjusting different risk-measurement parameters, distributed and risk-averse ADP algorithm can obtain decision results that adapt to various risk-aversion degrees. ADMM is introduced into the proposed algorithms to ensure data privacy between transmission system and multiple OWFs.

However, although the proposed DRADP algorithm exhibits more excellent computational performance than the conventional ADP algorithm, it still requires a large number of scenarios for training risk-averse AVFs. Thus, applying the risk-directed sampling method [35] to obtain scenarios from regions of high risk and reducing total number of required training scenarios to obtain converged risk-averse AVFs will be helpful to further increase computational efficiency, and it is a possible direction of future work.

APPENDIX A

The parameters of PSH and BS stations are listed in Table AI. The active load curve of the provincial power system, forecast scenario of wind speed in each OWF, and topology of each OWF are displayed in Figs. A1–A3, respectively. Total numbers of WTs in OWFs 1–4 are 160, 136, 146, and 127, respectively. The rated power of each WT is 8 MW, whereas the minimum power output is 0.103 MW. Cut-in wind speed, rated wind speed, and cut-out wind speed are 3, 13, and 25 m/s, respectively.

TABLE AI
PARAMETERS OF PSH STATIONS AND BS STATIONS

Storage unit	Maximum charge or pump power (MW)	Maximum discharge or generate power (MW)	Maximum stored energy (MWh)	Roundtrip efficiency
PSH1	2 400	2 400	27 252	77.1%
PSH2	1 200	1 200	16 456	76.0%
PSH3	2 400	2 400	34 065	78.0%
PSH4	1 280	1 280	18 000	76.0%
BS of OWF1	60	60	640	90%
BS of OWF2	40	40	560	90%
BS of OWF3	50	50	600	90%
BS of OWF4	32	32	500	90%

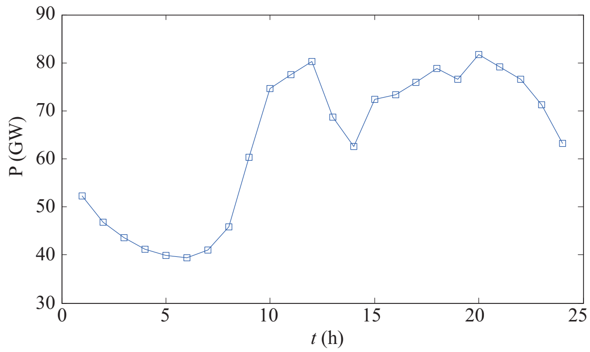

Fig. A1. Active load curve of the provincial power system.

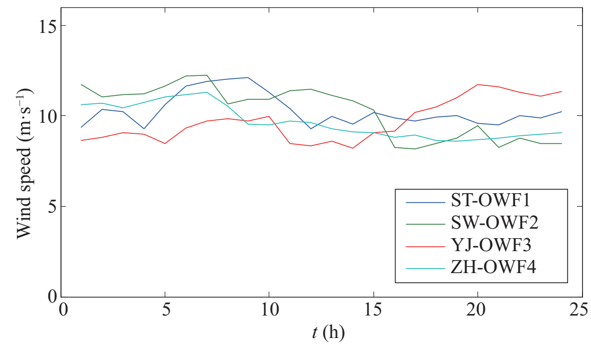

Fig. A2. Forecast scenario of the wind speed in each OWF.

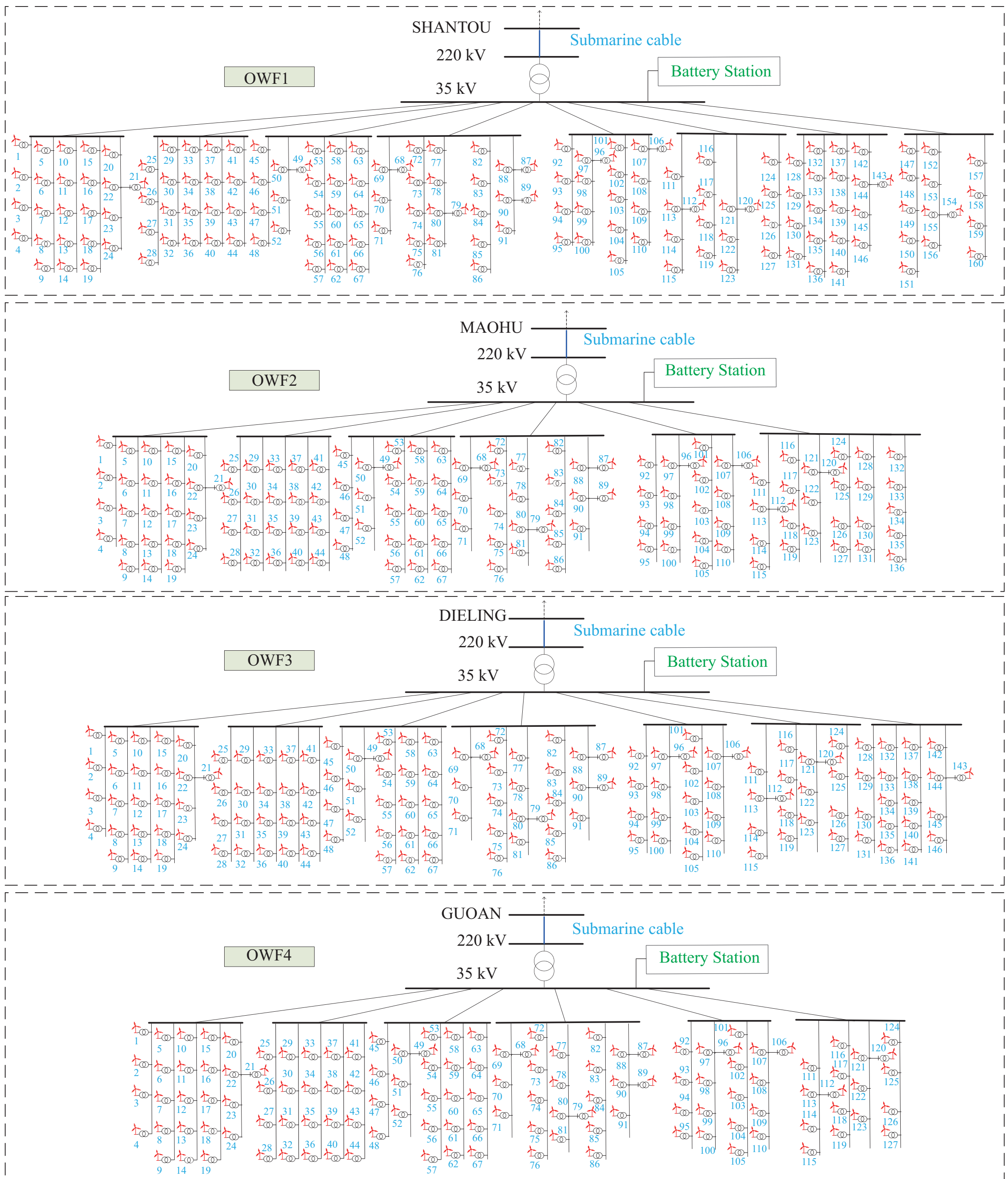

Fig. A3. Topology of each OWF.

REFERENCES

[1] Y. F. Guo, H. L. Gao, Q. W. Wu, H. R. Zhao, J. Østergaard, and M. Shahidehpour, "Enhanced voltage control of VSC-HVDC-connected offshore wind farms based on model predictive control," *IEEE Transactions on Sustainable Energy*, vol. 9, no. 1, pp. 474–487, Jan. 2018.

[2] A. Turk, Q. W. Wu, M. L. Zhang, and J. Østergaard, "Day-ahead stochastic scheduling of integrated multi-energy system for flexibility synergy and uncertainty balancing," *Energy*, vol. 196, pp. 117130, Apr. 2020.

[3] H. R. Zhao, Q. W. Wu, S. J. Hu, H. H. Xu, and C. N. Rasmussen, "Review of energy storage system for wind power integration support," *Applied Energy*, vol. 137, pp. 545–553, Jan. 2015.

[4] J. Li, Z. Y. Li, F. Liu, H. X. Ye, X. M. Zhang, S. W. Mei, and N. C. Chang, "Robust coordinated transmission and generation expansion planning considering ramping requirements and construction periods," *IEEE Transactions on Power Systems*, vol. 33, no. 1, pp. 268–280, Jan. 2018.

[5] M. Yang, M. Q. Wang, F. L. Cheng, and W. J. Lee, "Robust economic dispatch considering automatic generation control with affine recourse process," *International Journal of Electrical Power & Energy Systems*, vol. 81, pp. 289–298, Oct. 2016.

[6] W. B. Powell and S. Meisel, "Tutorial on stochastic optimization in energy—part I: modeling and policies," *IEEE Transactions on Power Systems*, vol. 31, no. 2, pp. 1459–1467, Mar. 2016.

[7] A. Sturt and G. Strbac, "Efficient stochastic scheduling for simulation of wind-integrated power systems," *IEEE Transactions on Power Systems*, vol. 27, no. 1, pp. 323–334, Feb. 2012.

[8] Y. T. Lin, T. Y. Ji, Y. Z. Jiang and Q. H. Wu, "Stochastic Economic Dispatch Considering the Dependence of Multiple Wind Farms Using Multivariate Gaussian Kernel Copula," *CSEE Journal of Power and Energy Systems*, vol. 8, no. 5, pp. 1352–1362, Sep. 2022.

[9] A. Dolatabadi, M. Jadidbonab, and B. Mohammadi-Ivatloo, "Short-term scheduling strategy for wind-based energy hub: a hybrid stochastic/IGDT approach," *IEEE Transactions on Sustainable Energy*, vol. 10, no. 1, pp. 438–448, Jan. 2019.

[10] Q. P. Zheng, J. H. Wang, and A. L. Liu, "Stochastic optimization for unit commitment—A review," *IEEE Transactions on Power Systems*, vol. 30, no. 4, pp. 1913–1924, Jul. 2015.

[11] J. W. Wang, C. Zhang, S. You, Y. Zong, C. Træholt, and Z. Y. Dong, "Multi-timescale coordinated operation of a CHP plant-wind farm portfolio considering multiple uncertainties," *International Journal of Electrical Power & Energy Systems*, vol. 125, pp. 106428, Feb. 2021.

[12] Z. M. Li, L. Wu, and Y. Xu, "Risk-averse coordinated operation of a multi-energy Microgrid considering Voltage/Var control and thermal flow: an adaptive stochastic approach," *IEEE Transactions on Smart Grid*, vol. 12, no. 5, pp. 3914–3927, Sep. 2021

[13] F. Farzan, M. A. Jafari, R. Masiello, and Y. Lu, "Toward optimal day-ahead scheduling and operation control of microgrids under uncertainty," *IEEE Transactions on Smart Grid*, vol. 6, no. 2, pp. 499–507, Mar. 2015.

[14] M. Daneshvar, H. Eskandari, A. B. Sirous, and R. Esmaeilzadeh, "A novel techno-economic risk-averse strategy for optimal scheduling of renewable-based industrial microgrid," *Sustainable Cities and Society*, vol. 70, pp. 102879, Jul. 2021.

[15] D. M. Yu, J. W. Wang, D. Z. Li, K. Jermsittiparsert, and S. Nojavan, "Risk-averse stochastic operation of a power system integrated with hydrogen storage system and wind generation in the presence of demand response program," *International Journal of Hydrogen Energy*, vol. 44, no. 59, pp. 31204–31215, Nov. 2019.

[16] A. Rabiee, A. Soroudi, and A. Keane, "Risk-averse preventive voltage control of AC/DC power systems including wind power generation," *IEEE Transactions on Sustainable Energy*, vol. 6, no. 4, pp. 1494–1505, Oct. 2015.

[17] R. Hemmati, H. Saboori, and S. Saboori, "Stochastic risk-averse coordinated scheduling of grid integrated energy storage units in transmission constrained wind-thermal systems within a conditional value-at-risk framework," *Energy*, vol. 113, pp. 762–775, Oct. 2016.

[18] J. Belles-Sampera, M. Guillén, and M. Santolino, "Beyond Value-at-risk: GlueVaR distortion risk measures," *Risk Analysis*, vol. 34, no. 1, pp. 121–134, Jan. 2014.

[19] S. J. Lin, G. S. Fan, G. Y. Jian, and M. B. Liu, "Stochastic economic dispatch of power system with multiple wind farms and pumped-storage hydro stations using approximate dynamic programming," *IET Renewable Power Generation*, 14(13): 2507–2516, Oct. 2020.

[20] Z. Shu and P. Jirutitijaroen, "Optimal operation strategy of energy storage system for grid-connected wind power plants," *IEEE Transactions on Sustainable Energy*, vol. 5, no. 1, pp. 190–199, Jan. 2014.

[21] H. Shuai, J. K. Fang, X. M. Ai, Y. F. Tang, J. Y. Wen, and H. B. He, "Stochastic optimization of economic dispatch for microgrid based on approximate dynamic programming," *IEEE Transactions on Smart Grid*, vol. 10, no. 3, pp. 2440–2452, May 2019.

[22] N. Zhang, B. D. Leibowicz, and G. A. Hanasusanto, "Optimal residential battery storage operations using robust data-driven dynamic programming," *IEEE Transactions on Smart Grid*, vol. 11, no. 2, pp. 1771–1780, Mar. 2020.

[23] Y. F. Guo, H. L. Gao, H. Xing, Q. W. Wu, and Z. W. Lin, "Decentralized coordinated voltage control for VSC-HVDC connected wind farms based on ADMM," *IEEE Transactions on Sustainable Energy*, vol. 10, no. 2, pp. 800–810, Apr. 2019.

[24] Y. Xiang, M. Q. Fang, J. Y. Liu, P. L, Zeng, P. Xue and G. Wu, "Distributed Dispatch of Multiple Energy Systems Considering Carbon Trading," *CSEE Journal of Power and Energy Systems*, vol. 9, no. 2, pp. 459–469, Mar. 2023.

[25] E. Ghadimi, A. Teixeira, I. Shames, and M. Johansson, "Optimal parameter selection for the alternating direction method of multipliers (ADMM): Quadratic problems," *IEEE Transactions on Automatic Control*, vol. 60, no. 3, pp. 644–658, Mar. 2015.

[26] Z. Chen, C. X. Guo, S. F. Dong, Y. Ding, and H. Y. Mao, "Distributed robust dynamic economic dispatch of integrated transmission and distribution systems," *IEEE Transactions on Industry Applications*, vol. 57, no. 5, pp. 4500–4512, Sep./Oct. 2021.

[27] S. Mhanna, G. Verbič, and A. C. Chapman, "Adaptive ADMM for distributed AC optimal power flow," *IEEE Transactions on Power Systems*, vol. 34, no. 3, pp. 2025–2035, May 2019.

[28] L. Jiang, "Convexity, translation invariance and subadditivity for g-expectations and related risk measures," *Annals of Applied Probability*, vol. 18, no. 1, pp. 245–258, Feb. 2008.

[29] H. Zhang, V. Vittal, G. T. Heydt, and J. Quintero, "A mixed-integer linear programming approach for multi-stage security-constrained transmission expansion planning," *IEEE Transactions on Power Systems*, vol. 27, no. 2, pp. 1125–1133, May 2012.

[30] X. Y. Feng, S. J. Lin, W. B. Liu, W. K. Liang and M. B. Liu, "Distributionally Robust Optimal Dispatch of Offshore Wind Farm Cluster Connected by VSC-MTDC Considering Wind Speed Correlation," *CSEE Journal of Power and Energy Systems*, vol. 9, no. 3, pp. 1021–1035, May 2023.

[31] M. Farivar and S. H. Low, "Branch flow model: relaxations and convexification—part I," *IEEE Transactions on Power Systems*, vol. 28, no. 3, pp. 2554–2564, Aug. 2013.

[32] P. Hou, W. H. Hu, M. Soltani, and Z. Chen, "Optimized placement of wind turbines in large-scale offshore wind farm using particle swarm optimization algorithm," *IEEE Transactions on Sustainable Energy*, vol. 6, no. 4, pp. 1272–1282, Oct. 2015.

[33] A. Ruszczyński, "Risk-averse dynamic programming for Markov decision processes," *Mathematical Programming*, vol. 125, no. 2, pp. 235–261, Jul. 2010.

[34] J. Nascimento and W. B. Powell, "An optimal approximate dynamic programming algorithm for concave, scalar storage problems with vector-valued controls," *IEEE Transactions on Automatic Control*, vol. 58, no. 12, pp. 2995–3010, Dec. 2013.

[35] Y. M. Wang, L. Wu, and S. X. Wang, "A fully-decentralized consensus-based ADMM approach for DC-OPF with demand response," *IEEE Transactions on Smart Grid*, vol. 8, no. 6, pp. 2637–2647, Nov. 2017.

[36] Z. N. Pan, T. Yu, J. Li, K. P. Qu, and B. Yang, "Risk-averse real-time dispatch of integrated electricity and heat system using a modified approximate dynamic programming approach," *Energy*, vol. 198, pp. 117347, May 2020.

[37] D. R. Jiang and W. B. Powell, "Risk-averse approximate dynamic programming with quantile-based risk measures," *Mathematics of Operations Research*, vol. 43, no. 2, pp. 554–579, Nov. 2017.

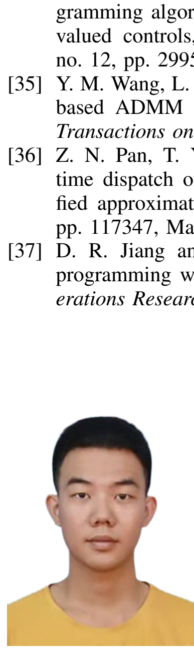

Xiangyong Feng received the B.S. degree in Electrical Engineering from the South China University of Technology in 2021, where he is currently pursuing his M.S. degree in Electrical Engineering. His research interests include power system optimization, operation, and control.

Shunjiang Lin received the B.S. degree in Electrical Engineering from South China University of Technology in 2003, and the Ph.D. degree in Electrical Engineering from Hunan University in 2008. He is currently an Associate Professor at the School of Electric Power Engineering, South China University of Technology. His research interests include power system optimization, operation, and control.

Yutao Liang received the B.S. degree in Electrical Engineering from South China University of Technology in 2022. He is currently pursuing the M.S. degree with the School of Electric Power Engineering, South China University of Technology. His research interests include power system optimization, operation, and control.

Guansheng Fan received the B.S. degree in Electrical Engineering from South China University of Technology in 2018, and received the M.S. degree in Electrical Engineering from South China University of Technology in 2021. His research interests include power system optimization, operation, and control.

Mingbo Liu received the B.S. degree from the Huazhong University of Science and Technology in 1985, the M.S. degree from the Harbin Institute of Technology in 1988, and the Ph.D. degree from Tsinghua University in 1992. He is currently a Professor at the South China University of Technology. He has authored and coauthored four monographs, two standards, and more than 280 articles. His research interests include energy management and operation control of power systems.